Mathematical Modeling and Numerical Simulation of Freezing Processes of a Supercooled Melt under Consideration of Density Changes

Michael Griebel
Institut für Angewandte Mathematik, Universität Bonn,
Wegelerstr. 6, 53115 Bonn

Willi Merz
Institut für Angewandte Mathematik, TU München,
Dachauerstr. 9a, 80335 München

Tilman Neunhoeffer
Institut für Informatik, TU München,
80290 München

Abstract

In this paper, we derive a model for the two-phase freezing process of supercooled fluids. Especially, we take density changes along the phase interfaces into account. Thus, besides heat diffusion and the interface phenomena, mass transport and convection in the fluid phase which is given by the full Navier–Stokes equations has to be considered.

For the 2D case we implemented an algorithm for the numerical solution of the mathematical model using uniform volume cells for a finite difference discretization. Additionally, the phase boundaries are captured by a surface tracking method.

We report on the mathematical model and its derivation, describe the numerical algorithm and present numerical experiments.

1 Introduction

Phase change processes are found almost everywhere in nature. Important examples are melting and freezing processes. They involve temperature distribution and transport by conduction and convection and are usually mathematically described by the well known Stefan formulation.

Typical areas of applications are the casting and solidification of melted iron or alloys, the freezing of water, the cooling of food and tissue, the latent heat thermal energy storage based on phase changing materials, or even cryosurgery [1].

For pure substances, there exist two substantially different kinds of solidification, see [24] and compare Figure 1. The classical Stefan problem models the solidification of a melt whose temperature is initially beyond the melting temperature T_m. The heat is extracted through the walls of the vessel with a temperature below T_m. Thus, the solidification front moves from the walls towards the center of the vessel. This process is completely stable.

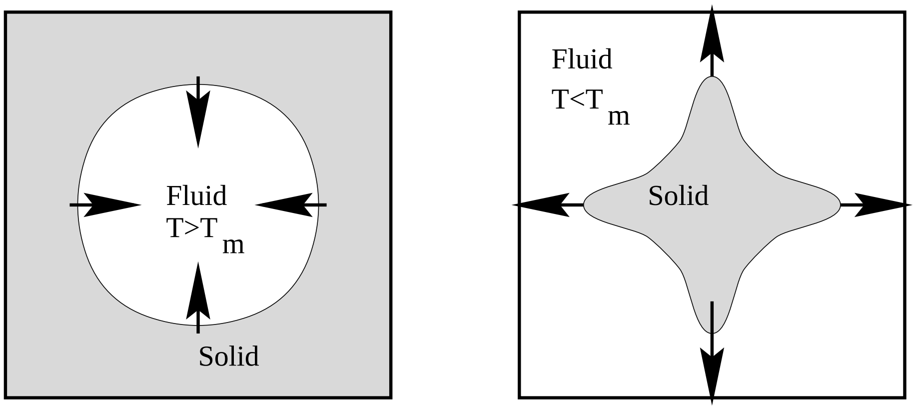

Figure 1: Solidification from the walls (left) and of a supercooled melt from a seed (right)

On the other hand, it is possible to cool many materials below the melting temperature without solidification. For example, water can be cooled down to $-40°$C before freezing. Moreover, some silicates or polymers can easily be supercooled by hundreds of degrees. Instead of crystallizing they turn into a glass-like state. The supercooled state is known to be thermodynamically metastable, i.e., the free energy is higher than that of the actual stable state of the solid. From the thermodynamical point of view, solidification requires an outflow of heat which changes the free energies, and therefore the relative thermodynamic stability of the different phases. If a nucleus is situated somewhere in the undercooled liquid, it will grow very rapidly.

Besides the thermal effects, we consider mass transport in this paper. This mass transport is caused by a density change during freezing. Water, for example, expands by about 10% during freezing whereas lithium shrinks by about 25%. Thus, some flow is initiated in the fluid. This fluid flow affects the whole solidification process, the shape of the crystal, and, for shrinking materials, there may even arise some cavities in the solid. In a closed container, these effects may cause serious containment problems.

In the *second section* of this paper, we derive a mathematical model for such freezing processes. It involves the Navier–Stokes equations in the fluid phase and the energy equation in both phases, resulting in a generalized two-phase Stefan problem coupled with fluid-dynamical effects. The free interface between the solid and the fluid phase is supplied with an extended version of the well known Gibbs–Thomson law describing the movement of the interface.

The numerical approach described in the *third section* consists of two parts. The first one determines the fluid velocity and the pressure by solving the Navier–Stokes equations in a time-dependent geometry. Here, we use Chorin's projection method or the SIMPLE scheme, combined with a finite difference discretization on an equidistant grid. The free boundaries

are described by a list of particles which are tracked with the computed velocities at the boundaries. By the help of these particles, the cells of the equidistant grid are divided into fluid cells and solid cells. The second part of the algorithm contains the computation of the temperature including the velocity of the solidification interface. Again, we apply a finite difference discretization on the grid which is also used for the fluid solver. Near the interfaces, the discretization is modified by the Shortley–Weller scheme.
Finally, we present some results of numerical experiments. Here, we study the convergence rates of our algorithm for a model problem, where an analytic solution is known. Furthermore, we consider the effects of density change for a seed with non-constant curvature and for water on a microscopic scale and give an example for dendritic crystal growth.

2 The Generalized Model

Commonly, solidification processes are modeled by the Stefan problem. The modeling of supercooled fluids also requires the Gibbs–Thomson law which gives a relation between the degree of supercooling, the curvature, and the velocity of the solid-liquid interface. However, density changes between solid and liquid are neglected in these models. Thus, no fluid-dynamical effects in the liquid are considered.
Here, we present an enlarged model, which includes the incompressible Navier–Stokes equations for the fluid phase, generalized Stefan and Gibbs–Thomson conditions, and an additional free boundary for the fluid caused by its movement.

2.1 Derivation of the generalized model

We consider an *open* container, in which the undercooled liquid is placed. Furthermore, a nucleus for the solidification process is situated in the container, consider Figure 2. $\Omega_L(t)$ denotes the fluid phase and $\Omega_S(t)$ the solid phase, $\Gamma_1(t)$ is the interface between liquid an solid phase, $\Gamma_2(t)$ is the free surface of the fluid, and Γ_3 denotes the solid wall of the container in which the fluid is placed. The normal unit vector $\vec{n}$ at $\Gamma_1(t)$ points into the liquid and, at the remaining boundaries, it points outward.
We start with the formulation of the classical conservation laws in the liquid and solid phase, i.e., we state equations conserving the total energy, the momentum, and the mass in the liquid phase. In the immobile solid phase, where the density is assumed to be constant, we just have to formulate the temperature equation.
The energy, momentum, and mass balance in the liquid phase $\Omega_L(t)$ are

$$\begin{aligned} \frac{\partial(\varrho_L\varepsilon)}{\partial t} + \operatorname{div}(\varrho_L\,\vec{v}\,\varepsilon) &= -\operatorname{div}(q_L - \mathcal{P}_L\,\vec{v})\,, && (1)\\ \frac{\partial(\varrho_L\vec{v})}{\partial t} + \operatorname{div}(\varrho_L\,\vec{v}\,\vec{v}) &= \operatorname{div}\mathcal{P}_L - \varrho_L\vec{g}\,, && (2)\\ \frac{\partial\varrho_L}{\partial t} + \operatorname{div}(\varrho_L\,\vec{v}) &= 0\,, && (3) \end{aligned}$$

respectively, where $\vec{v}$ is the velocity field of the fluid, ϱ_L its density, $\vec{g}$ denotes the gravity, $q_L = -k_L\,\nabla T$ is the conductive heat flux, and the total energy ε is defined as the sum of the

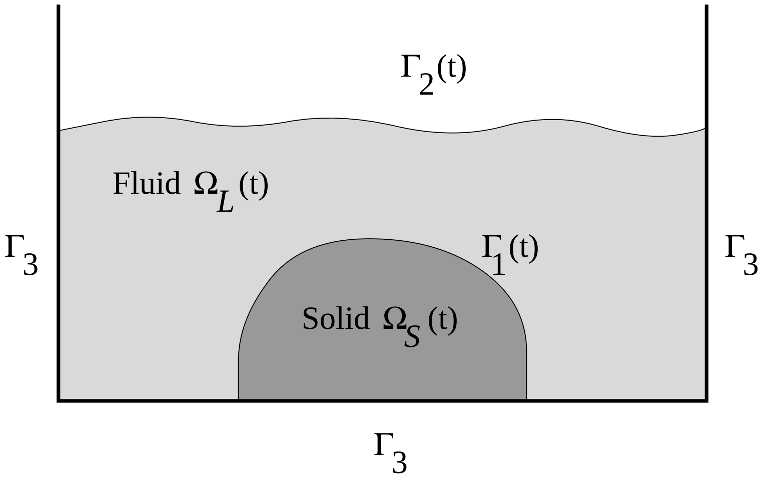

Figure 2: Configuration of the fluid container

internal energy u and the kinetic energy $|\vec{v}|^2/2$,

$$\varepsilon = u + |\vec{v}|^2/2\,.$$

$\mathcal{P}_L$ represents the stress tensor of the compressible Navier–Stokes equation, with the entries

$$\mathcal{P}_L^{ij} = -p_L\delta_{ij} + \mu_L\Big(\frac{\partial v_i}{\partial x_j} + \frac{\partial v_j}{\partial x_i}\Big) + (\lambda_L \mathrm{div}\,\vec{v})\,\delta_{ij}\,,$$

δ_{ij} being the Kronecker symbol for $i,j = 1,2$; μ_L and λ_L are the viscosities.
In the immobile solid phase $\Omega_S(t)$, we have $\vec{v} = 0$. Thus, just the temperature equation

$$\frac{\partial T}{\partial t} = \frac{k_S}{\varrho_S c_S}\,\triangle T \tag{4}$$

holds.
All the physical parameters, except the density ϱ_L of the fluid, are assumed to be constant. The quantities, such as specific heat capacity c, the conductivity k, the viscosities μ and λ, the density ϱ, and the pressure p, which are discontinuous across the boundary between the fluid and solid phase, are supplied with the subscripts L and S, respectively.
In buoyancy driven flows, it is common to approximate the exact compressible system by the Boussinesq approximation, where the densities are assumed to depend on the temperature and the pressure only, see [18].
So, in order to simplify the system of equations, we apply the Boussinesq approximation due to [21], assuming that the density is given by the constitutive equation

$$\varrho_L = \rho_L(1 - \alpha(T - T_m))\exp(\beta(p - p^*))\,,$$

where $\alpha := -\frac{1}{\varrho_L}\frac{\partial \varrho_L}{\partial T}$ is the coefficient of thermal expansion and $\rho_L := \varrho_L(T_m)$ is the reference density at the melting temperature. Since β, the fluid compressibility, is of order $O(10^{-5})$

and less for most of the melts (water, silicates) we are concerned with, we simply consider the linear relationship between the density and the temperature of the fluid

$$\hat{\varrho}_L(T) = \rho_L(1 - \alpha(T - T_m)) \, .$$

Following the approach in [18], it turns out that the terms containing the thermal expansion α (except in the gravitational force $\vec{g}$) can be neglected in order to approximate the system due to Boussinesq. Indeed, for supercooled water and silicates for instance, α is very small (it is of order $O(10^{-4})$).

In the case of constant density, the equations in the fluid simplify considerably. Putting the equations together (the energy equation can be written in terms of the internal energy u), we end up with the approximated system

$$\begin{aligned} \rho_L(\frac{\partial u}{\partial t} + \vec{v} \cdot \nabla u) &= -\operatorname{div} q_L, &(5)\\ \rho_L(\frac{\partial \vec{v}}{\partial t} + (\vec{v} \cdot \nabla)\vec{v}) &= -\nabla p_L + \mu_L \triangle \vec{v} + \hat{\varrho}(T)\vec{g}, &(6)\\ \operatorname{div}(\vec{v}) &= 0. &(7) \end{aligned}$$

Equation (4) in the solid phase remains unchanged.

But, if the density is constant, the internal energy u in the liquid phase may be expressed in terms of the temperature. Following the derivation in [1], we obtain $u = c_L(T - T_m)$, where c_L is assumed to be constant therein. Equation (5) thus reads as

$$\frac{\partial T}{\partial t} + \vec{v} \cdot \nabla T = \frac{k_L}{\varrho_L c_L} \triangle T \, . \tag{8}$$

Now, we have to supply the system with appropriate boundary conditions. The conditions on the container wall Γ_3 are obvious. The velocity field equals zero and the heat flux as well as the pressure gradient equal zero, too, since the container is insulated there. We have

$$\vec{v} = 0, \tag{9}$$

$$\nabla T \cdot \vec{n} = 0. \tag{10}$$

At the outer surface Γ_2, we take the usual stress balance for the Navier–Stokes equations, given by

$$-p\,\vec{n} + 2\mu_L \tau_L\,\vec{n} = -\gamma_2 \kappa_2\,\vec{n} - p^*\vec{n}\,, \tag{11}$$

where

$$\tau_L^{ij} = \frac{1}{2}\left(\frac{\partial v_L^i}{\partial x_j} + \frac{\partial v_L^j}{\partial x_i}\right), \qquad i,j = 1,2, \tag{12}$$

is the strain tensor, μ_L is the viscosity, γ_2 the surface tension, κ_2 the curvature, and p^* the atmospheric pressure. The sign of κ_2 is chosen such that it is positive for a convex fluid surface. The temperature flux at Γ_2 is

$$\frac{k_L}{\rho_L c_L}\,\nabla T \cdot \vec{n} = -h\,(T - T^*)\,, \tag{13}$$

where h is a flux parameter at the boundary. The velocity $\vec{V}_{\Gamma_2}$ of the free boundary is determined by the normal velocity of the particles situated there. So we simply have

$$\vec{V}_{\Gamma_2} \cdot \vec{n} = \vec{v} \cdot \vec{n}\,. \tag{14}$$

2.2 Conditions across the solid-liquid interface

The most interesting part concerning the boundary conditions is the free boundary Γ_1 between the fluid and the solid phase at which solidification occurs.
The basic assumption in view of Stefan problems treated in the literature (models for the Stefan problem with supercooling as well as some analysis and numerical experiments can be found in [5], [9], [10], [13], [16], [17] [28], [29] and in the extensive literature cited therein) is that of a common density in the solid and liquid phase. We do not consider this simplified case here and take into account, that there is a jump in the densities between the two phases. This density change causes a movement in the fluid which influences the phase change.
Since mass is conserved across the boundary Γ_1, we get from the conservation law

$$\vec{j}_L \cdot \vec{n} = \vec{j}_S \cdot \vec{n}, \tag{15}$$

with the mass flux ($\vec{n}$ is directed into the liquid) across the interface

$$\vec{j}_L \cdot \vec{n} = \rho_L(\vec{v} - \vec{V}_{\Gamma_1}) \cdot \vec{n}$$

for the liquid and

$$\vec{j}_S \cdot \vec{n} = -\rho_S \vec{V}_{\Gamma_1} \cdot \vec{n}$$

for the solid phase. V_{Γ_1} denotes the velocity of the interface. This implies

$$\vec{v} \cdot \vec{n} = (1 - \frac{\rho_S}{\rho_L})\, \vec{V}_{\Gamma_1} \cdot \vec{n}. \tag{16}$$

In order to complete the boundary conditions for the Navier–Stokes equations at Γ_1, we take

$$\vec{v} \cdot \vec{t} = 0, \tag{17}$$

$\vec{t}$ being the tangential vector at Γ_1.
Equation (4) requires the continuity condition

$$T_S = T_L \tag{18}$$

at the free interface.
Since $\rho_L \neq \rho_S$, we have to formulate the total energy balance across the free boundary. The energy content in the liquid and solid phase, i.e., in $\Omega_L(t) \cup \Omega_S(t)$, is given by

$$E(t) = \int_{\Omega_L(t) \cup \Omega_S(t)} \rho\, \varepsilon \, d\vec{x}. \tag{19}$$

Using the generalized transport theorem, see [6], we derive

$$\frac{d}{dt} E(t) = \int_{\Omega_L(t) \cup \Omega_S(t)} \rho \frac{d}{dt} \varepsilon \, d\vec{x} + \int_{\Gamma_1} [\rho\, \varepsilon (\vec{v} - \vec{V}_{\Gamma_1}) \cdot \vec{n}]_S^L \, d\Gamma \,, \tag{20}$$

where $[\cdot]_S^L$ denotes the jump across the boundary. Note that the unit normal vector $\vec{n}$ at Γ_1 is directed into the liquid. The conservation of energy across the boundary (see [6]) reads

$$\frac{d}{dt} E(t) = - \int_{\partial\Omega} q \cdot \vec{n} \, d\Gamma + \int_{\partial\Omega} \vec{n}^T \mathcal{P}\, \vec{v} \, d\Gamma + \int_{\Gamma_1} \psi \, d\Gamma \,, \tag{21}$$

where $\Omega = \Omega_L(t) \cup \Omega_L(t)$. The superscript T denotes the transposed vector and ψ is an additional source term at the free boundary. Using this with $\psi = \gamma_1 \kappa_1 \vec{V}_{\Gamma_1} \cdot \vec{n}$ and the energy equation (1), we get the boundary condition

$$[\rho \varepsilon (\vec{v} - \vec{V}_{\Gamma_1}) \cdot \vec{n} + q \cdot \vec{n} - \vec{n}^T \mathcal{P} \vec{v}]_S^L = -\gamma_1 \kappa_1 \vec{V}_{\Gamma_1} \cdot \vec{n}, \tag{22}$$

with $\varepsilon = u + |\vec{v}|^2/2$. As already stated, the internal energy u was set to

$$u_L = c_L(T - T_m)$$

in the liquid phase and to

$$u_S = c_S(T - T_m) - L$$

in the solid phase, L being the latent heat.

The second effect at the interface is the lowering of the freezing point at a curved interface, known as the Gibbs–Thomson effect. An essential requirement is that the temperature T depends on the kinematics of the interface. So we postulate on the boundary the constitutive relationship

$$T = T(\vec{V}_{\Gamma_1}, \kappa_1, p). \tag{23}$$

From the classical theory, see [20] for instance, it is known that

$$T(\vec{V}_{\Gamma_1}, \kappa_1, p) = T_m, \tag{24}$$

if $\vec{V}_{\Gamma_1} \cdot \vec{n} = 0$ and $\kappa_1 = 0$. From the Laplace–Young relation $p_S - p_L = \gamma_1 \kappa_1$, the relation $p_L = p_S =: p^*$ must hold, p^* being the atmospheric pressure. So, the phase change temperature T_m is the temperature at which the phases, separated by a planar interface, can coexist. Away from the equilibrium state, the Gibbs–Thomson relation approximates (23). In order to derive it, we use some basic physical laws following the ideas of [11].

Using the transport theorem again, we get the momentum transport across the free surface, which has the form

$$[\vec{v} (\vec{j} \cdot \vec{n}) - \vec{n}^T \mathcal{P}]_S^L = -\gamma_1 \kappa_1 \vec{n}. \tag{25}$$

We combine (22) and (25), write the internal energy in terms of the enthalpy e, i.e., $e = u + \frac{p}{\rho}$, to obtain

$$[(\vec{j} \cdot \vec{n}) (e + (\vec{v} - \vec{V}_{\Gamma_1})^2/2) + q \cdot \vec{n} - \vec{n}^T \tau (\vec{v} - \vec{V}_{\Gamma_1})]_S^L = 0, \tag{26}$$

where τ is the strain tensor (12).

The entropy production rate $\sigma(T)$ across Γ_1, a function of the temperature, is

$$\sigma(T) = [s (\vec{j} \cdot \vec{n}) - k \nabla (\ln T) \cdot \vec{n}]_S^L, \tag{27}$$

where s is the entropy. Combining this with (26) and the chemical potential $g = e - Ts$ gives

$$\sigma(T) = -\frac{(\vec{j} \cdot \vec{n})}{T} [g + \frac{(\vec{v} - \vec{V}_{\Gamma_1})^2}{2} - \frac{\vec{n}^T \tau \vec{n}}{\rho}]_S^L. \tag{28}$$

Neglecting the relative motion of the interface in (28), we postulate for the generalized chemical potential

$$G = g - \frac{\vec{n}^T \tau \vec{n}}{\rho}$$

the relationship in terms of the solid phase

$$a\,(\vec{j}_S \cdot \vec{n}) = -\frac{1}{T}\,[G]_S^L\,, \tag{29}$$

in analogy to [11]. This means that the jump of the generalized chemical potential across the interface controls the mass flux between the two phases; $a > 0$ is a kinetic coefficient. For the steady state, the jump is zero. This linear law implies

$$\sigma(T) = a\,(\vec{j}_S \cdot \vec{n})^2\,, \tag{30}$$

which ensures that the entropy production is nonnegative. From this, it is also evident that the surface entropy production is associated with the interface motion, implying that the chemical potentials are continuous across the interface only in a steady state (equilibrium) situation.
The "normal phase change temperature T_m" is determined as the temperature at which the free energy curves for liquid and solid intersect at atmospheric pressure p^*, satisfying

$$\Delta s = s_L - s_S = \frac{L}{T_m}\,,$$

see [1]. Using the standard thermodynamic relations

$$(\frac{\partial g}{\partial T})_p = -s$$

and

$$(\frac{\partial g}{\partial p})_T = -\frac{1}{\rho}\,,$$

we expand the chemical potentials around their melting temperature T_m and around the atmospheric pressure p^* to obtain the first order term

$$\frac{T - T_m}{T_m} = -\frac{1}{L}\,[g - \frac{p - p^*}{\rho}]_S^L\,.$$

From (28), this leads in terms of $j = j_S$ to

$$\frac{T - T_m}{T_m} = \frac{T_m \sigma}{L\,(\vec{j}_S \cdot \vec{n})} + \frac{1}{L}\Big[\frac{(\vec{v} - \vec{V}_{\Gamma_1})^2}{2} - \frac{\vec{n}^T\,\mathcal{P}\,\vec{n} + p^*}{\rho}\Big]_S^L\,. \tag{31}$$

Since the relative difference of the densities between the liquid and solid is small, we expand the last term of (31) with respect to the small quantity

$$\delta_\rho = \frac{\rho_S - \rho_L}{\rho_L}\,.$$

We use (15) and (25) and consider the first order terms in δ_ρ, i.e.,

$$\begin{aligned}\frac{1}{L}\Big[\frac{(\vec{v} - \vec{V}_{\Gamma_1})^2}{2} &- \frac{\vec{n}^T\,\mathcal{P}\,\vec{n} + p^*}{\rho}\Big]_S^L = \\ &- \frac{\gamma_1 \kappa_1}{L\,\rho_S} - \frac{\rho_S - \rho_L}{L\,\rho_S \rho_L}\,(\vec{n}^T\,\mathcal{P}_L\,\vec{n} + p^*) + O(\frac{\tilde{\rho}\,(\vec{v} - \vec{V}_{\Gamma_1})^2}{L}).\end{aligned} \tag{32}$$

Due to [11], the kinetic energy contribution $O(\tilde{\delta}_\rho\,(\vec{v}-\vec{V}_{\Gamma_1})^2/L)$ in the previous equation is negligible in all practical cases (it would change the freezing point by 1K only for interface velocities as high as 10m/s). Using (30) and (31), we get the Gibbs–Thomson law on Γ_1, which has the form

$$\frac{T-T_m}{T_m} = -\frac{\gamma_1\kappa_1}{L\,\rho_S} - \frac{a\,\rho_S\,T_m}{L}\,\vec{V}_{\Gamma_1}\cdot\vec{n} - \frac{\rho_S-\rho_L}{L\,\rho_S\,\rho_L}\,(\vec{n}^T\,\mathcal{P}_L\,\vec{n}+p^*)\,. \tag{33}$$

The first term on the right hand side of equation (33) corresponds to the usual Gibbs–Thomson law. The variation of the freezing point is given by the capillarity length $\frac{\gamma_1}{L\rho_S}$ and the curvature κ_1. The Mullins–Sekerka analysis which studies the morphological stability shows that supercooling destabilizes planar interfaces while the surface tension in the first term acts as a stabilizing force. The competition between these two effects guarantees the great variety of observed morphologies. We also note that this term is very small in general (except for large curvature). So, this term is insignificant for the heat transfer process, but it is important for the morphology of the growing interface. Examples can be found in [1].
The second term in (33) brings in the dynamics, describing the nonequilibrium situation due to the motion of the interface. In many papers, the appearance of this term is justified only on an ad hoc basis.
The last term varies the freezing point due to the density changes and due to the pressure in the system.

2.3 The Model

In this section we briefly summarize the previous results and state the complete model in compact form.
In the liquid phase $\Omega_L(t)$, we have the set of equations

$$\begin{aligned}
\frac{\partial T}{\partial t} + \operatorname{div}(\vec{v}\,T) &= \frac{k_L}{\rho_L c_L}\,\triangle T\,, && (34)\\
\rho_L\Big(\frac{\partial\vec{v}}{\partial t} + \nabla(\vec{v}\otimes\vec{v})\Big) &= -\nabla p_L + \mu_L\triangle\vec{v} + \hat{\varrho}(T)\vec{g}\,,^{1} && (35)\\
\operatorname{div}(\vec{v}) &= 0\,. && (36)
\end{aligned}$$

Here, we applied the continuity equation (36) to get the conservative formulation of the convective terms in (34) and (35) from (6) and (8).
In the immobile solid phase $\Omega_S(t)$, where $\vec{v}=0$, the temperature distribution is given by

$$\frac{\partial T}{\partial t} = \frac{k_S}{\varrho_S c_S}\,\triangle T. \tag{37}$$

The boundary conditions at Γ_1 consist of the condition

$$[\,\varepsilon\,(\vec{j}\cdot\vec{n}) + q\cdot\vec{n} - \vec{n}^T\,\mathcal{P}\,\vec{v}]_S^L = -\gamma_1\kappa_1\,\vec{V}_{\Gamma_1}\cdot\vec{n}\,, \tag{38}$$

for the temperature equation in the liquid and

[1] $\vec{v}\otimes\vec{v}$ denotes the tensor product of two vectors which gives a matrix with elements $(\vec{v}\otimes\vec{v})_{i,j} := v_i v_j$.

$$T_S = T_L \tag{39}$$

for the temperature equation in the solid, since the temperature across the boundary is continuous. For the Navier–Stokes equation we have

$$\begin{aligned} \vec{v}\cdot\vec{n} &= (1-\frac{\rho_S}{\rho_L})\,\vec{V}_{\Gamma_1}\cdot\vec{n}\,, &(40)\\ \vec{v}\cdot\vec{t} &= 0. &(41)\end{aligned}$$

The movement of the interface Γ_1 is described by the Gibbs–Thomson law, which has the form

$$\frac{T-T_m}{T_m} = -\frac{\gamma_1\kappa_1}{L\,\rho_S} - \frac{a\,\rho_S\,T_m}{L}\,\vec{V}_{\Gamma_1}\cdot\vec{n} - \frac{\rho_S-\rho_L}{L\,\rho_S\,\rho_L}\,(\vec{n}^T\,\mathcal{P}_L\,\vec{n}+p^*)\,. \tag{42}$$

At Γ_2, we have for the temperature and the momentum equation

$$\begin{aligned} \frac{k_L}{\rho_L c_L}\nabla T\cdot\vec{n} &= -h(T-T^*)\,, &(43)\\ -p\,\vec{n}+2\mu_L\tau_L\,\vec{n} &= -\gamma_2\kappa_2\,\vec{n}-p^*\vec{n}\,. &(44)\end{aligned}$$

The movement of Γ_2 is described by

$$\vec{V}_{\Gamma_2}\cdot\vec{n} = \vec{v}\cdot\vec{n}\,. \tag{45}$$

At Γ_3, the conditions are

$$\begin{aligned} \nabla T\cdot\vec{n} &= 0\,, &(46)\\ \vec{v} &= 0\,. &(47)\end{aligned}$$

Moreover, we have to supply the system with appropriate initial data for the temperature in both phases and for the velocity field in the liquid phase.

3 The numerical algorithm

In literature, many algorithms for simulating the solidification of supercooled liquids *without* density changes are described. Thus, the fluid motion is neglected in those models. Moreover, the parameters in the fluid and in the solid are assumed to be equal. Then, the model is reduced to the energy equation (37) which holds in the solid and the liquid phase. In (38), the velocity dependent terms on the left hand side vanish because of $c_L = c_S$ and $\vec{v} = 0$. It remains the classical Stefan condition

$$k(\nabla T_S - \nabla T_L)\cdot\vec{n} = \rho L\vec{V}_{\Gamma_1}\cdot\vec{n}. \tag{48}$$

Moreover, the pressure dependent term vanishes in the Gibbs–Thomson law (42). The reduced model is completed by some boundary data (46) for the temperature on the container wall Γ_3.

Most work is done in two space dimensions using the enthalpy formulation [33], front tracking [34], level set formulations combined with boundary integral methods [30], phase field models [8],[9],[15], and variational algorithms [2], among others. In recent times, there are also simulations in three space dimensions using the finite difference enthalpy method [35], the phase field model [23], and adaptive finite element techniques with separate meshes for the computation of the interface location and the temperature [29].
But, as far as we know, there is only the ELAFINT algorithm for simulating solidification processes of supercooled fluids including density changes in 2D, [32]. However, the mathematical model is much simpler than the one we derived in this paper. Especially the kinetic terms in the Gibbs–Thomson equation are omitted there.

3.1 Survey of the algorithm

Our 2D algorithm to approximate the solution of the model presented in the previous section couples two separate algorithms. The first part is a Navier–Stokes solver for the computation of the velocities and the pressure in the fluid. It is based on a finite difference discretization on a fixed staggered grid. The pressure velocity coupling is solved by Chorin's projection method [14] or the SIMPLE method [26]. As boundary data for the velocity on the solid-liquid interface, we use (47), applying special interpolation techniques as reported in [36]. The free surface is treated with the surface marker method [12].

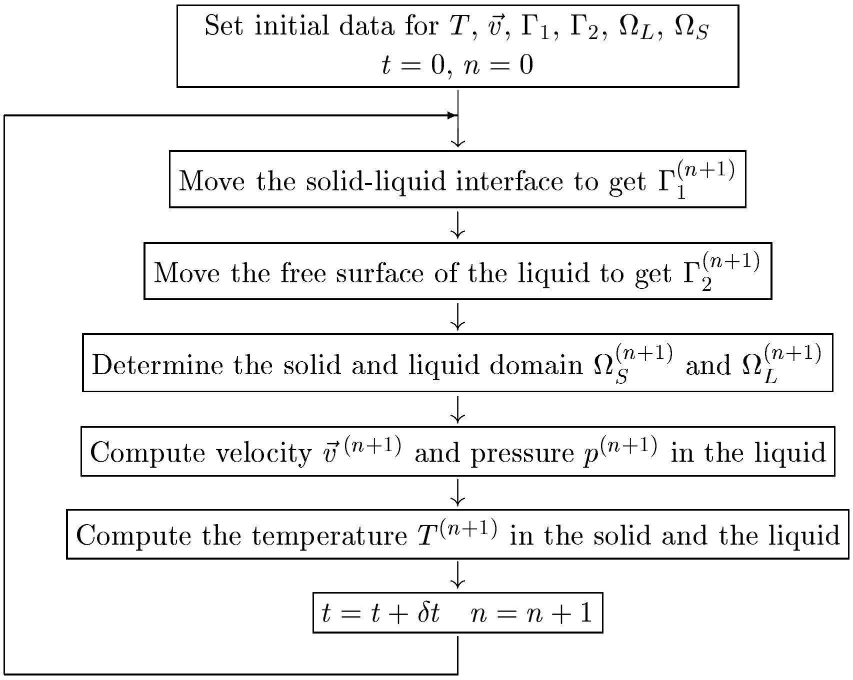

Figure 3: Flowchart of the whole algorithm

On the other hand, the algorithm to compute the temperature distribution is based on a finite difference discretization of (37) and (34). We use the same grid as for the Navier–Stokes solver and special discretization techniques at the solid-liquid interface. The temperature

at this interface described by a polygon is given by a combination of the generalized Stefan and the Gibbs–Thomson condition (38) and (42). The interface is tracked with the velocity calculated by use of the Gibbs–Thomson law (42). This algorithm is also capable of solving the solidification without density changes. An overview of the whole algorithm is given in Figure 3.
The fluid solver affects the temperature in the convective term of the energy equation in the fluid (34) and the movement of the free fluid surface Γ_2. On the other hand, the temperature influences the fluid solver by the movement of the solid-liquid interface Γ_1 and the resulting boundary condition for the fluid velocity (40).

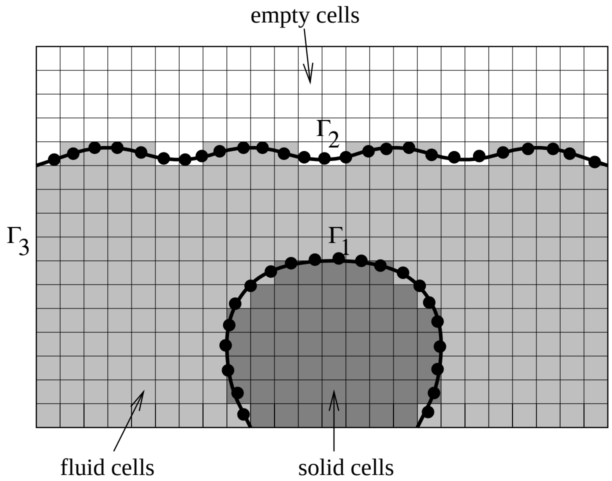

Figure 4: Decomposition of the base domain Ω_0 into solid, liquid and empty cells

The staggered grid used for both, the Navier–Stokes equations and the energy equations, is defined as follows. The rectangular base domain $\Omega_0 := [0, a] \times [0, b]$ of the container is covered with a grid containing $i_{\max} \times j_{\max}$ cells of equal size where the gridlines are spaced by a distance of $\delta x := a/i_{\max}$ in x-direction and $\delta y := b/j_{\max}$ in y-direction. The cells are divided into solid cells, liquid cells and empty cells for that part of the container which is not occupied by the solid or the fluid (see Figure 4). Decisive for the cell type is the domain in which the midpoint of the cell is situated. The cell types are specified in an integer array. This array is set in the initialization phase. In each time step, we determine the cells which have changed their type after moving the boundaries, and we set the integer array accordingly.
The discrete temperature $T_{i,j}$ and pressure $p_{i,j}$ are located at the midpoint of the cell $C_{i,j} := [(i-1)\delta x, i\delta x] \times [(j-1)\delta y, j\delta y]$ whereas the discrete horizontal velocity component $u_{i,j}$ of $\vec{v} = (u, v)^T$ is located at the midpoint of the right vertical edge of $C_{i,j}$ and the discrete vertical velocity component $v_{i,j}$ is located at the midpoint of the upper horizontal edge of $C_{i,j}$ (see Figure 5). The time interval is divided into sub-intervals $[t^{(n)}, t^{(n+1)}]$ with step size $\delta t := t^{(n+1)} - t^{(n)}$. We denote velocity, pressure and temperature values at time t_n by an upper index (n).
The free boundaries Γ_1 between the solid and the liquid phase as well as the surface of the liquid Γ_2 are given by a list of points $\vec{\zeta}_k, k = 1, \ldots, n_1$ and $\vec{\zeta}_k, k = n_1 + 1, \ldots, n_1 + n_2$, respectively, which are connected by circular arcs. The arc between $\vec{\zeta}_k$ and $\vec{\zeta}_{k+1}$ is defined by

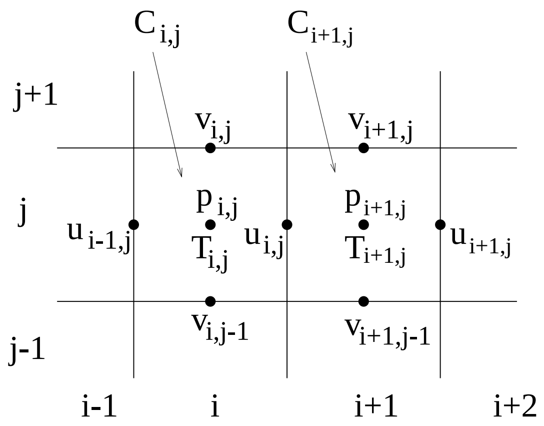

Figure 5: Location of the discrete values in the staggered grid

the location of the two points and the mean value of the curvatures of the arcs through $\vec{\zeta}_{k-1}$, $\vec{\zeta}_k$, $\vec{\zeta}_{k+1}$ and through $\vec{\zeta}_k$, $\vec{\zeta}_{k+1}$, $\vec{\zeta}_{k+2}$.
In the initialization phase, the points are set equidistant. After moving the boundaries, one should assure that the distances between two points are not too big. If they exceed a certain value which should be less than or equal to the grid sizes δx and δy, one has to add a new point in the list by interpolation of the neighboring point locations.
In the following we describe the two parts of the algorithm in more detail.

3.2 The algorithm for velocity and pressure in the liquid

The velocity and the pressure in the liquid are calculated by Chorin's projection method or, alternatively, the SIMPLE method. Here, the time derivative is discretized by a simple Euler step. In the time step $t^{(n)} \to t^{(n+1)}$, we first compute an intermediate velocity field $\vec{v}^{\,*}$ by means of the momentum equation (35). For Chorin's projection method, we use an explicit time discretization and $\vec{v}^{\,*}$ can be computed directly by

$$\vec{v}^{\,*} = \vec{v}^{\,(n)} + \delta t \left(\frac{\mu_L}{\rho_L} \triangle \vec{v}^{\,(n)} - \nabla(\vec{v}^{\,(n)} \otimes \vec{v}^{\,(n)}) - \frac{1}{\rho_L} \nabla p^{(n)} + \frac{\hat{\varrho}(T^{(n)})}{\rho_L} \vec{g} \right). \tag{49}$$

The SIMPLE algorithm uses a semi-implicit time discretization. Here, $\vec{v}^{\,*}$ is calculated as the solution of the linear convection-diffusion equation

$$\vec{v}^{\,*} + \delta t \left(-\frac{\mu_L}{\rho_L} \triangle \vec{v}^{\,*} + \nabla(\vec{v}^{\,(n)} \otimes \vec{v}^{\,*}) \right) = \vec{v}^{\,(n)} + \delta t \left(-\frac{1}{\rho_L} \nabla p^{(n)} + \frac{\hat{\varrho}(T^{(n)})}{\rho_L} \vec{g} \right). \tag{50}$$

Afterwards, the intermediate velocity field is corrected by the gradient of a pressure correction term to obtain the velocity at time step $t^{(n+1)}$

$$\vec{v}^{\,(n+1)} = \vec{v}^{\,*} - \frac{\delta t}{\rho_L} \nabla\, \delta p^{(n+1)}, \tag{51}$$

$$p^{(n+1)} = p^{(n)} + \delta p^{(n+1)}. \tag{52}$$

The continuity equation (36) for $\vec{v}^{\,(n+1)}$ gives a Poisson equation for the pressure correction term:

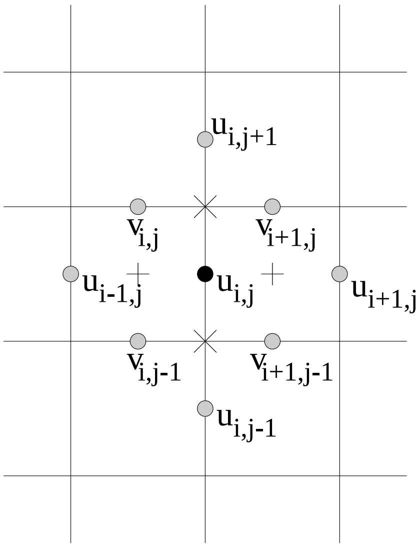

Figure 6: Velocity values needed for discretization of the first component of the momentum equation

$$\triangle \delta p^{(n+1)} = \frac{\rho_L}{\delta t} \nabla \cdot \vec{v}^{\,*}. \tag{53}$$

The space derivatives are discretized by central differences at the midpoints of edges between two fluid cells. The first component of the vector equation (49) is discretized at the midpoints of the vertical edges and the second component is discretized at the midpoints of the horizontal edges. As an example, we give the discretization formulas for the first component of (49) at the midpoint of the right vertical edge of cell $C_{i,j}$. The convective parts are discretized using mean values of u^2 at the cell midpoints marked with "+" and by mean values of uv at the cell corners marked with "×" in Figure 6:

$$[\triangle u]_{i,j} \;:=\; \frac{u_{i+1,j} - 2\,u_{i,j} + u_{i-1,j}}{\delta x^2} + \frac{u_{i,j+1} - 2\,u_{i,j} + u_{i,j-1}}{\delta y^2}, \tag{54}$$

$$\left[\frac{\partial(u^2)}{\partial x} + \frac{\partial(uv)}{\partial y}\right]_{i,j} \;:=\; \frac{(u_{i+1,j} + u_{i,j})^2 - (u_{i,j} + u_{i-1,j})^2}{4\,\delta x} + \frac{(u_{i,j+1} + u_{i,j})(v_{i+1,j} + v_{i,j}) - (u_{i,j} + u_{i,j-1})(v_{i+1,j-1} + v_{i,j-1})}{4\,\delta y}. \tag{55}$$

The Poisson equation for the pressure (53) is discretized in the center of each fluid cell $C_{i,j}$ by

$$\frac{p_{i+1,j} - 2p_{i,j} + p_{i-1,j}}{\delta x^2} + \frac{p_{i,j+1} - 2p_{i,j} + p_{i,j-1}}{\delta y^2} = \frac{\rho_L}{\delta t} \left(\frac{u^*_{i,j} - u^*_{i-1,j}}{\delta x} + \frac{v^*_{i,j} - v^*_{i,j-1}}{\delta y} \right), \tag{56}$$

which can be solved by any iterative method for the solution of large linear systems. We use successive overrelaxation (SOR) in our simulations.

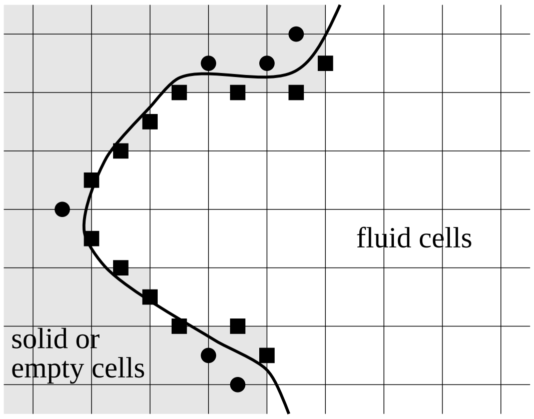

Figure 7: Necessary boundary data at grid edges

It remains to determine the boundary values for $\vec{v}$ and p. At Γ_1 and Γ_3, the velocity $\vec{v}$ is directly given by the Dirichlet conditions (40), (41), and (47). At the free surface of the fluid Γ_2, we have the coupled boundary condition (44).
The discretization formulas (54) and (55), which are applied to all edges between two fluid cells, require velocity values at edges between fluid cells and non-fluid cells (squares in Figure 7) and at edges between two non-fluid cells neighboring fluid cells (circles in Figure 7). These values are obtained by linear interpolation between the given value at the boundary and the value at the nearest fluid edge, compare the GENSMAC code [36].
Consider for example the situation given in Figure 8. The horizontal velocity component $u_{i,j}$ at the edge between the fluid cell $C_{i,j}$ and the solid cell $C_{i+1,j}$ is computed using the boundary value u_r at the intersection point of the boundary and the dashed horizontal center line of $C_{i,j}$ and the fluid value $u_{i-1,j}$. The vertical velocity component $v_{i+1,j}$ between the two solid cells $C_{i+1,j}$ and $C_{i+1,j+1}$ is computed using the boundary value v_r at the intersection point of the boundary and the gridline $x = j \cdot \delta y$ and the fluid value $v_{i,j}$.
To determine the pressure and the velocity at the free surface, we locally transform (44) into polar coordinates (r, ϕ) at each point of the discrete free surface $\vec{\zeta}_k$, $k = n_1 + 1, \ldots, n_1 + n_2$. The midpoint of this polar coordinate system is defined as the midpoint of the circle through the three free surface points $\vec{\zeta}_{k-1}$, $\vec{\zeta}_k$ and $\vec{\zeta}_{k+1}$. Thus, if we approximate the free surface locally by an arc through these three points, r=constant holds on the arc.
The strain tensor τ (12) reads in polar coordinates as

$$\tau = \frac{1}{2} \begin{pmatrix} 2\,\dfrac{\partial \hat{u}}{\partial r} & r\,\dfrac{\partial}{\partial r}\left(\dfrac{\hat{v}}{r}\right) + \dfrac{1}{r}\dfrac{\partial \hat{u}}{\partial \phi} \\ r\,\dfrac{\partial}{\partial r}\left(\dfrac{\hat{v}}{r}\right) + \dfrac{1}{r}\dfrac{\partial \hat{u}}{\partial \phi} & 2\left(\dfrac{1}{r}\dfrac{\partial \hat{v}}{\partial \phi} + \dfrac{\hat{u}}{r}\right) \end{pmatrix}, \tag{57}$$

where $\hat{u}$ is the radial velocity component and $\hat{v}$ is the tangential velocity component.
Multiplying (57) by the normal $\vec{n}$ and the tangential unit vector $\vec{t} := (-n_2, n_1)^T$, we obtain

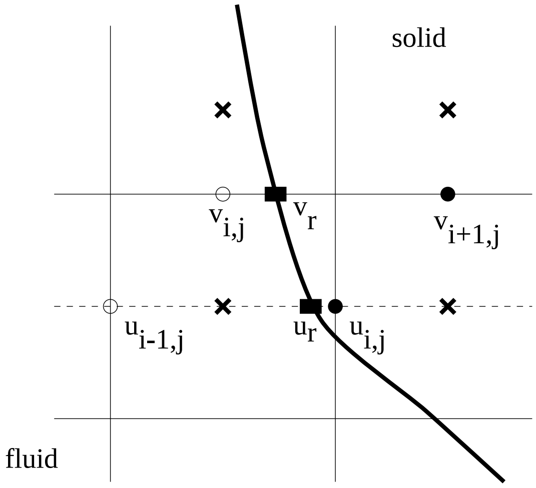

Figure 8: Interpolation of boundary values

$$-(p - p^*) + 2\,\mu\,\frac{\partial \hat{u}}{\partial r} \;=\; -\gamma_2\,\kappa_2, \tag{58}$$

$$\frac{\partial \hat{v}}{\partial r} - \frac{\hat{v}}{r} + \frac{1}{r}\frac{\partial \hat{u}}{\partial \phi} \;=\; 0. \tag{59}$$

We discretize (59) by

$$\frac{\hat{v}_k - \hat{v}_{k,fluid}}{\delta r} - \frac{\hat{v}_k}{r} + \frac{\hat{u}_{k+1} - \hat{u}_{k-1}}{r\delta\phi} = 0, \tag{60}$$

where $\hat{v}_{k,fluid}$ is the tangential velocity at $\vec{x}_{k,fluid} := \vec{\zeta}_k - \delta r\,\vec{n}_k$ and $\delta\phi$ is the angle between the lines connecting the midpoint of the circle with $\vec{\zeta}_{k-1}$ and $\vec{\zeta}_{k+1}$, see Figure 9. The fluid velocity $\hat{v}_{k,fluid}$ is obtained by bilinear interpolation of the surrounding grid values of u and v. These grid values are located at the corners of the rectangles emphasized by shading in the figure.
Together with the continuity equation in polar coordinates

$$\frac{\partial \hat{u}}{\partial r} + \frac{\hat{u}}{r} + \frac{1}{r}\frac{\partial \hat{v}}{\partial \phi} = 0 \tag{61}$$

which is discretized in the same manner, we get a linear system for the velocity values $\hat{u}_k$ and $\hat{v}_k$ at the discrete free surface points $\vec{\zeta}_k$, $k = n_1 + 1, \ldots, n_1 + n_2$. This non-definite system can be solved by Kaczmarz iterations [22].
Afterwards, we can compute the pressure at the free surface by discretizing $\frac{\partial \hat{u}}{\partial r}$ in (58), and we transform the velocity values back to cartesian coordinates.
For the discretization of the spatial derivatives at the edges between two fluid cells adjacent to empty cells, we now need velocity values at the midpoints of the edges between fluid and empty cells and at edges between two empty cells adjacent to fluid cells. These values are

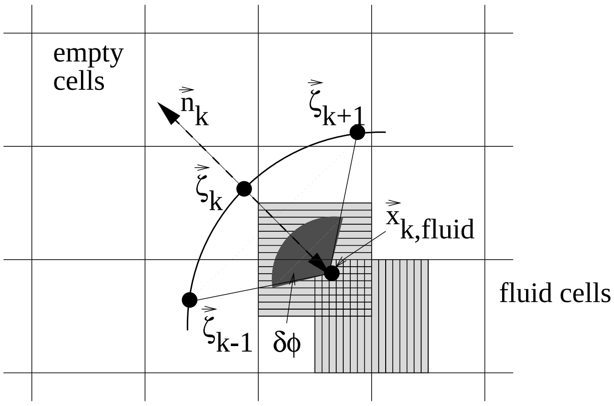

Figure 9: Discretization of the boundary conditions at the free surface

obtained by interpolation of the values at the boundaries and values in the fluid as it is described on page 15 for boundaries of solid obstacles.
After the computation of the velocity values, the points of the free surface $\vec{\zeta}_k$, $k = n_1 + 1, \ldots, n_1 + n_2$, are tracked with the velocities u_k and v_k.
In order to ensure the stability of the explicit time stepping algorithm in Chorin's projection method and not to generate oscillations, we must obey the following stability conditions for the stepsizes δx, δy and dt, the so called Friedrichs–Courant–Lewy (CFL) conditions.

$$\frac{2\delta t\, \mu_L}{\rho_L} < \left(\frac{1}{dx^2} + \frac{1}{\delta y^2} \right)^{-1}, \tag{62}$$

$$|u_{max}|\, \delta t < \delta x, \qquad |v_{max}|\, \delta t < \delta y, \tag{63}$$

where $|u_{max}|$ and $|v_{max}|$ denote the maximal absolute values of u and v occurring in the grid. The SIMPLE algorithm only requires to obey (63), which says that a particle in the fluid moves not more than a grid cell in one time step. This condition is necessary because of the moving boundaries, where initial values are required in new fluid cells.

3.3 The algorithm for the temperature

The energy equations in the solid (37) and in the liquid (34) are solved in an implicit time stepping scheme. The boundary data for the temperature on Γ_2 and Γ_3 is given by (43) and (46), respectively. On Γ_1, we have (39) together with the generalized Stefan condition and the Gibbs–Thomson condition (38) and (42). Resolving (42) for $V_{\Gamma_1} := \vec{V}_{\Gamma_1} \cdot \vec{n}$ and using the abbreviations

$$\varepsilon_\kappa := \frac{\gamma_1 T_m}{L\rho_s}, \qquad \varepsilon_V := \frac{a\rho_s T_m^2}{L}, \qquad \varepsilon_p := \frac{T_m}{L} \left(\frac{1}{\rho_S} - \frac{1}{\rho_L} \right), \tag{64}$$

we obtain an expression for the velocity of the solid-liquid interface

$$V_{\Gamma_1} = \frac{1}{\varepsilon_V} \left(T_m - T - \varepsilon_\kappa\, \kappa - \varepsilon_p \left(p - p^* - 2\,\mu \frac{\partial \hat{u}}{\partial r} \right) \right). \tag{65}$$

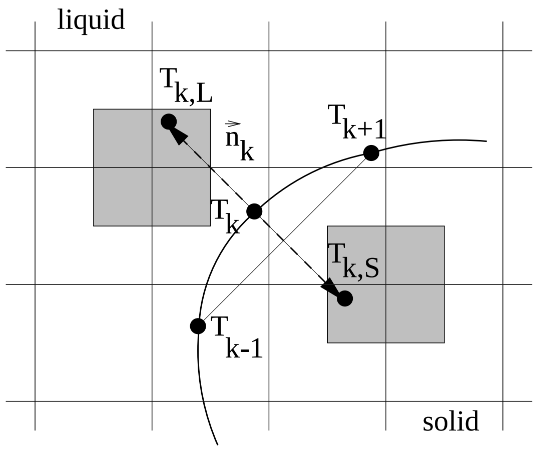

Figure 10: Discretization of the Stefan condition

The kinetic term $\vec{n}^T \tau\, \vec{n}$ is evaluated in polar coordinates as shown in (57), resulting in the normal derivative of the normal velocity component $\partial\hat{u}/\partial r$.
Writing the generalized Stefan condition (38) in terms of the temperature T and neglecting the term with the kinetic energy which is of cubic order in V_{Γ_1},[2] we get

$$\begin{aligned} k_S \frac{\partial T}{\partial n}\Big|_S - k_L \frac{\partial T}{\partial n}\Big|_L &+ \\ \rho_L\, c_L\, (T - T_m)(\vec{v}\cdot\vec{n} - V_{\Gamma_1}) + \rho_S\, c_S\, (T - T_m)\, V_{\Gamma_1} &+ \\ p_L\, \vec{v}\cdot n - 2\,\mu\, \frac{\partial \hat{u}}{\partial r}\, \vec{v}\cdot\vec{n} &= (\rho_S\, L - \gamma_1\, \kappa_1) V_{\Gamma_1}. \end{aligned} \tag{66}$$

We now substitute $\vec{v}\cdot\vec{n}$ by the right hand side of (40) and V_{Γ_1} by the right hand side of (65). Thus, we obtain a boundary condition for T on Γ_1 only containing T in linear and quadratic terms, the normal derivatives of T, and the velocity derivative $\partial\hat{u}/\partial r$, which is discretized as the derivative at the fluid surface in (60).
The normal derivatives of T at a point $\vec{\zeta}_k$ of the interface Γ_1 are discretized by

$$[\nabla T_S\cdot\vec{n}]_k := \frac{T_k - T_{k,S}}{\delta}, \quad [\nabla T_L\cdot\vec{n}]_k := \frac{T_{k,L} - T_k}{\delta}, \quad k = 1,\ldots,n_1, \tag{67}$$

where $T_k := T(\vec{\zeta}_k)$, $T_{k,S} := T(\vec{\zeta}_k - \delta\vec{n}_k)$, and $T_{k,L} := T(\vec{\zeta}_k + \delta\vec{n}_k)$. The temperature values in the solid and in the liquid $T_{k,S}$ and $T_{k,L}$ are determined by bilinear interpolation from the four surrounding values $T_{i,j}$ at cell centers (see Figure 10, the rectangles for the bilinear interpolations are shaded). Because of the jump in the temperature gradient along the interface, the stepsize δ must be chosen such that the values needed for interpolation are all in the same phase. This is guaranteed by $\delta = \sqrt{\delta x^2 + \delta y^2}$.
Alternatively to the linear approximation of the normal derivatives in (67), one can also use the second order discretization

[2] If we would not neglect this term, we would end with a cubic equation for the temperature at each particle instead of the quadratic equation mentioned below.

$$[\nabla T_S \cdot \vec{n}]_k := \frac{3T_k - 4T_{k,S} + T_{k,S,2}}{2\delta}, \quad [\nabla T_L \cdot \vec{n}]_k := \frac{-T_{k,L,2} + 4T_{k,L} - 3T_k}{2\delta}, \quad k = 1, \ldots, n_1, \tag{68}$$

where $T_{k,S,2} := T(\vec{\zeta}_k - 2\delta\vec{n}_k)$ and $T_{k,L,2} := T(\vec{\zeta}_k + 2\delta\vec{n}_k)$ are the temperatures at a distance 2δ from $\vec{\zeta}_k$. These two values are also determined by bilinear interpolation from the surrounding grid values. Numerical experiments in Section 4 show much better results for this quadratic approximation. But, for very fine structures as they arise in the computation of dendrites for example, this approximation is not useful because temperature values of the wrong phase might be included for the interpolation of $T_{k,S,2}$ or $T_{k,L,2}$.
Applying one of these two discretizations, (66) represents an equation for the temperature T_k which is linear in T_k if $c_L = c_S$. Otherwise it is quadratic. Here, we take the solution which is closer to the melting temperature at planar interfaces T_m.
The boundary values at the free surface of the fluid Γ_2 (43) are discretized in a same manner, leading to a linear equation for T_k at $\vec{\zeta}_k$, $k = n_1 + 1, \ldots, n_1 + n_2$.
The energy equations in the solid and the liquid phase are discretized as follows:

$$\begin{aligned} \frac{T_{i,j}^{(n+1)} - T_{i,j}^{(n)}}{\delta t} \quad = \quad & \frac{k_L}{\rho_L c_L} \left(\frac{T_{i+1,j}^{(n+1)} - 2\,T_{i,j}^{(n+1)} + T_{i-1,j}^{(n+1)}}{\delta x^2} + \frac{T_{i,j+1}^{(n+1)} - 2\,T_{i,j}^{(n+1)} + T_{i,j-1}^{(n+1)}}{\delta y^2} \right) - \\ & \frac{u_{i,j}^{(n+1)}(T_{i+1,j}^{(n+1)} + T_{i,j}^{(n+1)}) - u_{i-1,j}^{(n+1)}(T_{i,j}^{(n+1)} + T_{i-1,j}^{(n+1)})}{2\delta x} - \\ & \frac{v_{i,j}^{(n+1)}(T_{i,j+1}^{(n+1)} + T_{i,j}^{(n+1)}) - v_{i,j-1}^{(n+1)}(T_{i,j}^{(n+1)} + T_{i,j-1}^{(n+1)})}{2\delta y}, \end{aligned} \tag{69}$$

if $C_{i,j}$ is a fluid cell and

$$\frac{T_{i,j}^{(n+1)} - T_{i,j}^{(n)}}{\delta t} \quad = \quad \frac{k_S}{\rho_S c_S} \left(\frac{T_{i+1,j}^{(n+1)} - 2\,T_{i,j}^{(n+1)} + T_{i-1,j}^{(n+1)}}{\delta x^2} + \frac{T_{i,j+1}^{(n+1)} - 2\,T_{i,j}^{(n+1)} + T_{i,j-1}^{(n+1)}}{\delta y^2} \right), \tag{70}$$

if $C_{i,j}$ is a solid cell.
Whenever temperatures at points in different phases enter the discrete energy equation for a certain grid point, we have to modify the discretization scheme because of the jump in the temperature gradient at the interface. To this end, we use a Shortley–Weller approximation of the derivatives for domains where the boundary does not coincide with gridlines [31]. Here the temperature T_Γ at the intersection point between the interface and a grid line is taken into account. This is obtained by interpolation of the temperatures of the nearest interface points $\vec{\zeta}_k$ and $\vec{\zeta}_{k+1}$. The Shortley–Weller scheme is based on difference quotients for non-equidistant grid points. As an example, we suppose that the interface intersects the line connecting the centers of the cells $C_{i,j}$ and $C_{i+1,j}$ (see Figure 11). Here, we discretize $\partial^2 T/\partial x^2$ by

$$\left[\frac{\partial^2 T}{\partial x^2}\right]_{i,j} = \frac{2\,T_{\Gamma,i,j}}{\delta r_{i,j}(\delta r_{i,j} + \delta x)} - \frac{2\,T_{i,j}}{\delta r_{i,j}\delta x} + \frac{2\,T_{i-1,j}}{\delta x(\delta r_{i,j} + \delta x)} \tag{71}$$

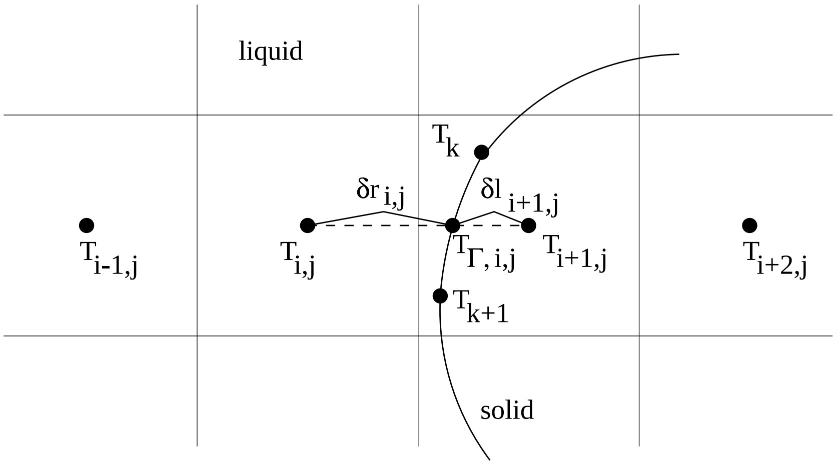

Figure 11: Shortley–Weller discretization near the interface

in the left hand cell $C_{i,j}$ and by

$$\left[\frac{\partial^2 T}{\partial x^2}\right]_{i+1,j} = \frac{2\,T_{i+2,j}}{\delta x(\delta l_{i+1,j}+\delta x)} - \frac{2\,T_{i+1,j}}{\delta l_{i+1,j}\delta x} + \frac{2\,T_{\Gamma,i,j}}{\delta l_{i+1,j}(\delta l_{i+1,j}+\delta x)} \tag{72}$$

in the right hand cell $C_{i+1,j}$. The discretization of the convective part in the fluid $\partial(uT)/\partial x$ is replaced by

$$\left[\frac{\partial(uT)}{\partial x}\right]_{i,j} = \frac{u_{\Gamma_i,j}T_{\Gamma,i,j} - u_{i-1,j}(T_{i,j}+T_{i-1,j})/2}{\delta x/2 + \delta r_{i,j}} \tag{73}$$

in the fluid cell $C_{i,j}$. That is, we replace the value of uT at the midpoint of the right vertical edge of cell $C_{i,j}$ by the value at the interface, changing the distance between the discretization points from δx to $\delta x/2 + \delta r_{i,j}$. The interface velocity u_Γ is given by an interpolation of the interface velocities at $\vec{\zeta}_k$ and $\vec{\zeta}_{k+1}$. The discretization of the derivatives in y-direction is done analogously. The same formulas are applied for the discretization of the energy equation near the free surface of the liquid Γ_2.

Altogether, we get a system of equations for the temperatures $T_{i,j}$ in the solid cells (70) and in the liquid cells (69), eventually modified near the free boundaries as described in (71), (72), and (73). For T_k, $k = 1, \ldots, n_1$, at the solid-liquid interface Γ_1 we have (66) and for T_k, $k = n_1+1, \ldots, n_1+n_2$, at the free surface Γ_2 we have the discretized version of (43). This system of equations can be solved by any iterative solver. We use the SOR algorithm in our simulations as for the solution of the pressure equation (56).

The tracking of the interface is realized by the Euler step

$$\vec{\zeta}_k^{(n+1)} = \vec{\zeta}_k^{(n)} + \delta t (V_{\Gamma_1})_k\, \vec{n}_k, \quad k = 1, \ldots n_1, \tag{74}$$

where $(V_{\Gamma_1})_k$ is given by (65).

The interface velocity V_{Γ_1} depends on the curvature of the interface κ_1. Therefore, an explicit time discretization using $(V_{\Gamma_1})_k^{(n)}$ requires to obey the stability condition

$$\frac{2\,\delta t\,\varepsilon_\kappa}{\varepsilon_V} < \Delta^2, \tag{75}$$

where $\Delta := \min_k\{||\vec{\zeta}_k - \vec{\zeta}_{k+1}||\}$ denotes the shortest distance between two neighboring particles, see [34].

To circumvent this restrictive condition for the time step size, an implicit time discretization with respect to curvature, which depends on the position of the particles, is recommended. For solving this implicit set of equation, we use a Picard iteration to determine the new positions of the particles $\vec{\zeta}_k^{(n+1)}$. The new iterate $\vec{\zeta}_k^{it+1}$ is computed by using the curvature of the old iterates $\vec{\zeta}_l^{it}, l = k-1, k, k+1$:

$\vec{\zeta}^{0} := \vec{\zeta}^{(n)}, \kappa^0 := \kappa^{(n)}$
for $it = 1, 2, \ldots, it_{\max}$
  for $k = 1, \ldots, n_1$
    compute κ_k^{it} using $\vec{\zeta}_{k-1}^{it}, \vec{\zeta}_k^{it}, \vec{\zeta}_{k+1}^{it}$,
    $V_k^{it} = -\frac{1}{\varepsilon_V}\left(T_k^{(n)} - T_m + \varepsilon_\kappa \kappa_k^{it} + \varepsilon_p(p_k^{(n)} - p^\star + 2\,\mu\,\partial\hat{u}^{(n)}/\partial r)\right)$,
    $\vec{\zeta}_k^{it+1} = \vec{\zeta}_k^{it} - \lambda\left(\vec{\zeta}_k^{it} - \vec{\zeta}_k^{(n)} - \delta t\,V_k^{it}\,\vec{n}\right)$,
  end for
  if norm of residual $< \epsilon$
    $\vec{\zeta}_k^{(n+1)} = \vec{\zeta}_k^{it+1}$ and stop iteration.
  end if
end for

The relaxation parameter λ is necessary to ensure convergence. It must be reduced whenever the iteration tends to diverge, i.e., if the norm of the residual $\vec{r}_k^{it} := \vec{\zeta}_k^{it} - \vec{\zeta}_k^{(n)} - \delta t\,V_k^{it}\,\vec{n}, k = 1, \ldots, n_1$, increases from one iteration step to the next.

4 Numerical experiments

Now, we present some numerical results of the algorithm described in Section 3. First, we consider a special example with a circular solid-liquid interface. Here, under certain assumptions, an analytic solution is known. We compare the error of the algorithm on several grid sizes. The second example treats the solidification of a non-circular seed. Here, the influence of non-constant curvature can be studied. In the third experiment, we consider the solidification of water on a microscopic scale. We conclude with an example for dendritic solidification.

Some more numerical results can be found in [25], especially concerning the example with known analytic solution. There, we also show separate results of the fluid and the temperature solver.

4.1 Example 1: convergence for a special configuration

According to [29], we first compare the results of our numerical algorithm with a known analytic solution for the problem with $\varepsilon_p = 0$, omitting the kinetic term $2\,\mu\,\partial\hat{u}/\partial r\,\vec{v}\cdot\vec{n}$ and the curvature dependent term $\gamma_1 \kappa_1 V_{\Gamma_1}$ in the generalized Stefan condition (66), and applying a special right hand side for the energy equation. Namely,

$$
\begin{aligned}
T(\vec{x},t) &:= \begin{cases} T_{\text{ice}}(t), & |\vec{x}| \le R_1(t), \\ T_{\text{ice}}(t) - \dfrac{e^{1/4}}{2}\displaystyle\int_1^{|\vec{x}|/R(t)} \dfrac{e^{-z^2/4}}{z}dz, & R_1(t) < |\vec{x}| \le R_2(t), \end{cases} \\
\vec{v}(\vec{x},t) &:= \left(1 - \frac{\rho_S}{\rho_L}\right)\frac{1}{|\vec{x}|^2}\vec{x}, \qquad R_1(t) < |\vec{x}| < R_2(t), \\
p(\vec{x},t) &:= -\frac{\rho_l}{8|\vec{x}|^2}\left(1 - \frac{\rho_S}{\rho_L}\right)^2 + p_0, \qquad R_1(t) < |\vec{x}| < R_2(t), \\
V_{\Gamma_1}(t) &:= \frac{1}{2R_1(t)}, \\
\Gamma_1(t) &:= \{\vec{x} \in \mathbb{R}^2, |\vec{x}| = R_1(t)\}, \\
\Gamma_2(t) &:= \{\vec{x} \in \mathbb{R}^2, |\vec{x}| = R_2(t)\},
\end{aligned}
$$

where

$$
\begin{aligned}
R_1(t) &:= \sqrt{R_{1,0}^2 + t}, \\
R_2(t) &:= \sqrt{R_{2,0}^2 + \left(1 - \frac{\rho_S}{\rho_L}\right)t}, \\
T_{\text{ice}}(t) &:= -\frac{1.5\varepsilon}{R_1(t)}, \\
p_0 &:= \frac{\gamma_2}{R_2(t)} - \left(\mu\left(1 - \frac{\rho_S}{\rho_L}\right) - \frac{\rho_L}{8}\left(1 - \frac{\rho_S}{\rho_L}\right)^2\right)\frac{1}{R_2(t)^2}
\end{aligned}
$$

is a solution of our problem with

$$
\varepsilon_\kappa = \varepsilon_V =: \varepsilon, \qquad \varepsilon_p = 0, \qquad k_L = k_S = c_L = c_S = 1, \qquad L = 1, \qquad \vec{g} = 0, \qquad p^* = 0.
$$

Moreover, we changed the condition for the temperature on the free surface Γ_2 into a Dirichlet boundary condition and we set the right hand side of the temperature equations (1) and (4) to

$$
\begin{aligned}
F_L(\vec{x},t) &:= \frac{0.75\varepsilon}{R_1(t)^3} - \frac{1}{2|\vec{x}|}e^{(1-\frac{|\vec{x}|}{R_1(t)})^2/4}, \qquad R_1(t) < |\vec{x}| \le R_2(t), \\
F_S(\vec{x},t) &:= \frac{0.75\varepsilon}{R_1(t)^3}, \qquad |\vec{x}| \le R_1(t).
\end{aligned}
$$

$R_{1,0}$ and $R_{2,0}$ are the initial radii of the circular interfaces Γ_1 and Γ_2 centered in $\vec{x}_0 = (0,0)$. In the numerical experiment, we set $\Omega = [-0.5, 0.5]^2$, $R_{1,0} = 0.15$, $R_{2,0} = 0.45$, $\varepsilon = 0.001$, $\rho_s = 1$, and $\rho_l = 1.5$, which leads to a volume expansion of 33 percent during solidification. The exact solution is shown in Figure 12.

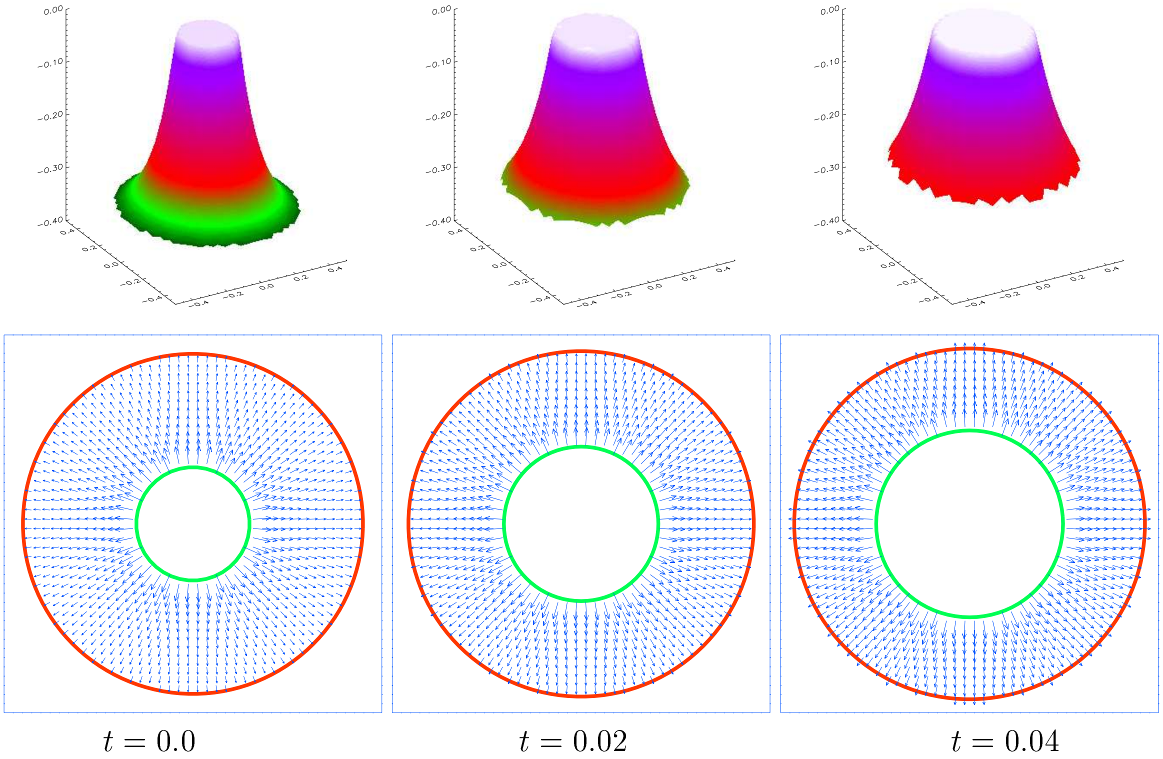

Figure 12: Example 1: Temperature, first row, and velocity field with solid-liquid interface (green) and free fluid surface (red), second row

	T		u		Γ_1		Γ_2	
$i_{\max}$	$\mathrm{err}_{i_{\max}}$	$\frac{\mathrm{err}_{i_{\max}/2}}{\mathrm{err}_{i_{\max}}}$	$\mathrm{err}_{i_{\max}}$	$\frac{\mathrm{err}_{i_{\max}/2}}{\mathrm{err}_{i_{\max}}}$	$\mathrm{err}_{i_{\max}}$	$\frac{\mathrm{err}_{i_{\max}/2}}{\mathrm{err}_{i_{\max}}}$	$\mathrm{err}_{i_{\max}}$	$\frac{\mathrm{err}_{i_{\max}/2}}{\mathrm{err}_{i_{\max}}}$
20	1.1e-1	—	2.9e-1	—	9.5e-2	—	8.2e-3	—
40	6.9e-2	1.6	1.7e-1	1.7	5.3e-2	1.8	4.9e-3	1.7
80	3.9e-2	1.8	9.0e-2	1.9	3.0e-2	1.8	2.7e-3	1.8
160	2.7e-2	1.5	5.5e-2	1.6	2.1e-2	1.4	1.6e-3	1.7

Table 1: Example 1: L^2-errors at $t = 0.04$, linear approximation of the derivatives in the Stefan condition

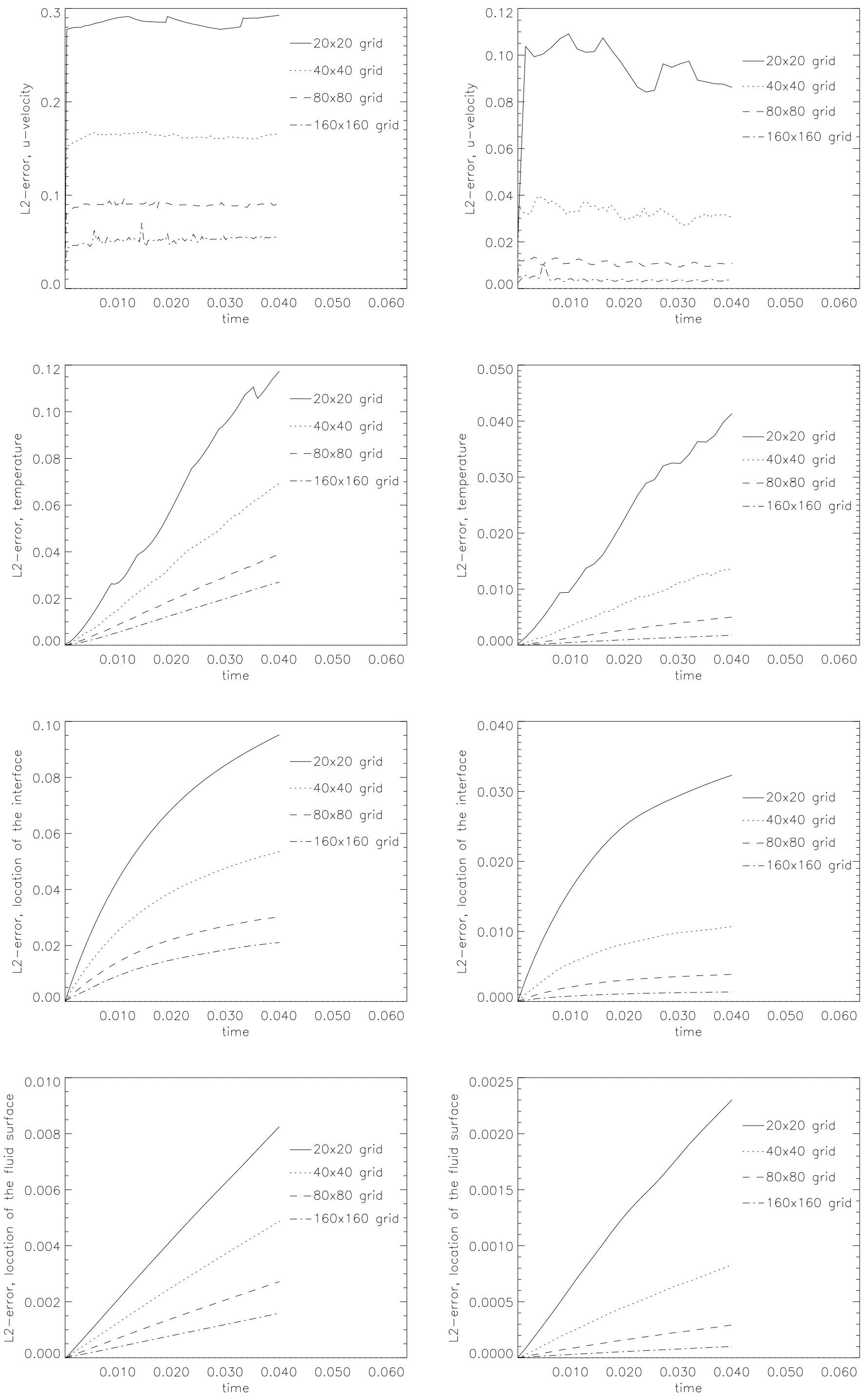

Figure 13: Example 1: L^2-errors in time for linear (left) and quadratic (right) approximation of the derivatives in the Stefan condition

$i_{\max}$	T $\text{err}_{i_{\max}}$	T $\frac{\text{err}_{i_{\max}/2}}{\text{err}_{i_{\max}}}$	u $\text{err}_{i_{\max}}$	u $\frac{\text{err}_{i_{\max}/2}}{\text{err}_{i_{\max}}}$	Γ_1 $\text{err}_{i_{\max}}$	Γ_1 $\frac{\text{err}_{i_{\max}/2}}{\text{err}_{i_{\max}}}$	Γ_2 $\text{err}_{i_{\max}}$	Γ_2 $\frac{\text{err}_{i_{\max}/2}}{\text{err}_{i_{\max}}}$
20	4.1e-2	—	8.6e-2	—	3.2e-2	—	2.3e-3	—
40	1.4e-2	2.9	3.1e-2	2.8	1.1e-2	2.9	8.3e-4	2.8
80	5.0e-3	2.8	1.1e-2	2.8	3.9e-3	2.8	2.9e-4	2.9
160	1.8e-3	2.8	3.7e-3	3.0	1.4e-3	2.8	1.0e-4	2.9

Table 2: Example 1: L^2-errors at $t = 0.04$, quadratic approximation of the derivatives in the Stefan condition

In Figure 13 and Tables 1 and 2, we show the errors for the velocity component u, the temperature T, and the locations of the solid-liquid interface Γ_1 and the free surface of the fluid Γ_2. We always present the relative discrete L^2-errors, that is the L^2-norm of the difference between computed approximation and analytic solution divided by the L^2-norm of the analytic solution. For the velocity error, we sum over all vertical edges between two fluid cells, for the temperature error, we sum over all fluid and solid cells, and for the errors of the boundaries, we take the sum over all particles.
We compare the errors on grids with $i_{\max} = 20$, 40, 80, and 160, using the linear and the quadratic approximation of the normal temperature derivatives in the Stefan condition (67) and (68), respectively. The related time step sizes are $\delta t = 0.00016, 0.0008, 0.0004$ and 0.0002. For the pressure velocity coupling, we used Chorin's projection method.
As we can see, the linear approximation results in a convergence rate less than $O(\delta x)$, whereas in the quadratic approximation, the errors show a convergence rate of about $O(\delta x^{3/2})$. Thus, the approximation of the normal derivatives in the Stefan condition has a great influence on all components of the solution. However, we do not get a $O(\delta x^2)$ convergence because the time discretization and the discretization of the movement of the boundaries are only of first order. Please note the different scales in Figure 13 in the left and right column.

4.2 Example 2: Different fluid densities and seed with non-constant curvature

In Example 2, we use a non-circular seed and consider the effect of non-constant curvature on the solidification process. Here the initial seed is a perturbed circle

$$\begin{pmatrix} x(s) \\ y(s) \end{pmatrix} = \Big(R_{1,0} + P\,\cos(2\,\pi\,k\,s)\Big)\begin{pmatrix} \cos(2\,\pi\,s) \\ \sin(2\,\pi\,s) \end{pmatrix}, \qquad s \in [0,1], \tag{76}$$

with average radius $R_{1,0} = 0.15$, perturbation size $P = 0.06$, and perturbation frequency $k = 4$, compare [30]. The initial form of the fluid surface is again a circle with radius $R_{2,0} = 0.375$. Besides the fluid density which will be varied in the following, we use the same parameters as in Example 1, also $\rho_S = 1$.
In contrast to Example 1, the right hand side F of the energy equations is set to zero. The

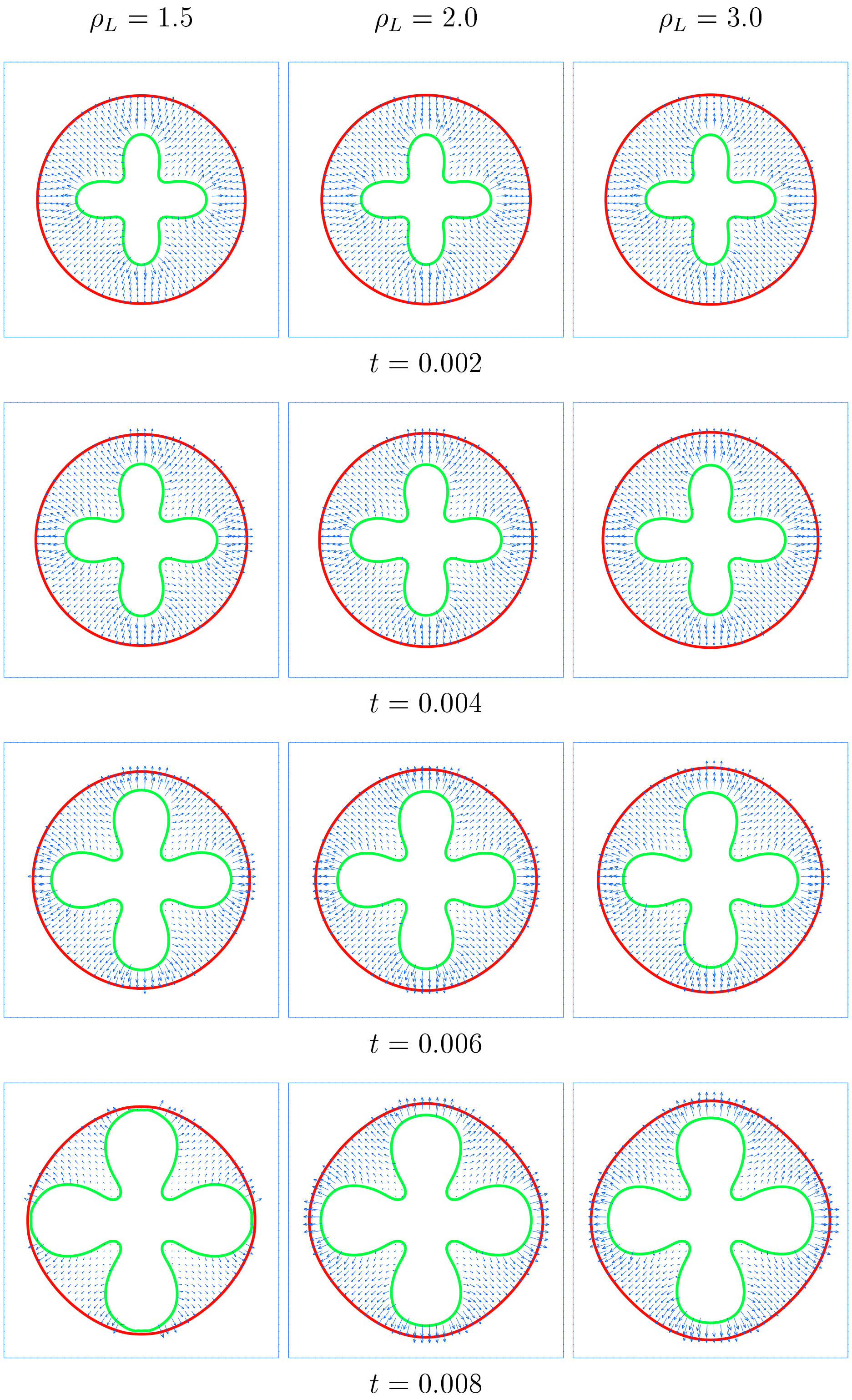

Figure 14: Example 2: Velocity field (blue), solid-liquid interface (green), and free fluid surface (red) for different fluid densities, the length of the velocity vectors is not uniformly scaled

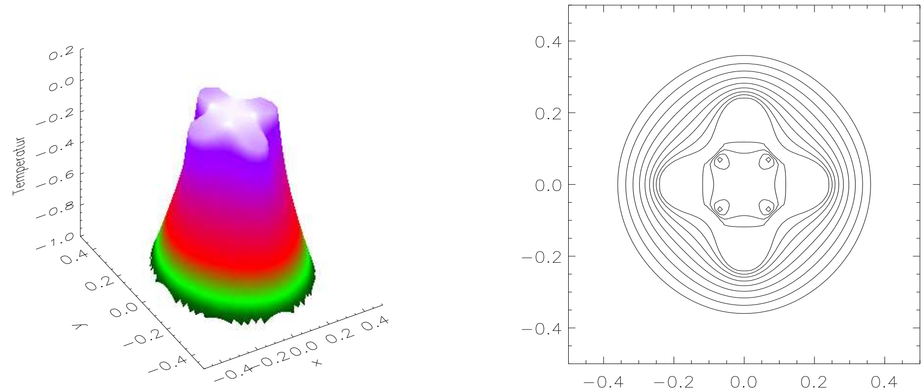

$t = 0.002$

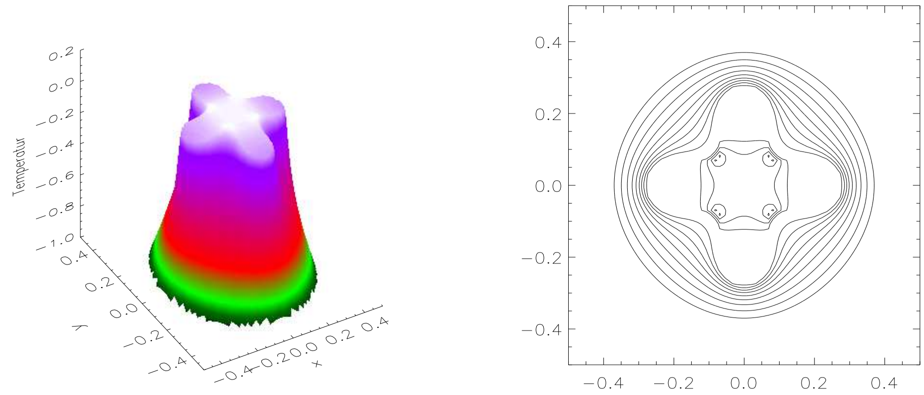

$t = 0.004$

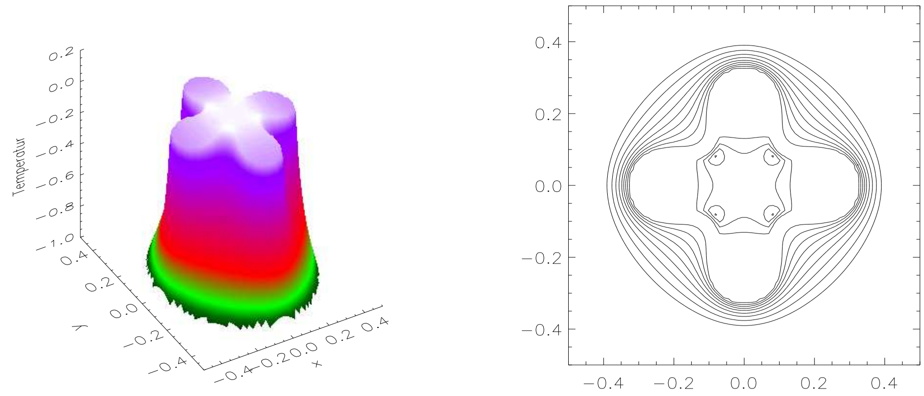

$t = 0.006$

Figure 15: Example 2: Temperature, surface plot and contour lines, $\rho_L = 2$

initial continuous temperature $T^{(0)}$ is computed by solving a Laplace equation with boundary conditions $T^{(0)} = -\varepsilon\kappa_1$ on Γ_1 and $T^{(0)} = -1.0$ on Γ_2.
In Figure 14, we show the velocity field and the boundaries at several time steps for $\rho_L = 1.5, 2$ and 3, computed on a grid with 80×80 cells with time step $t = 0.0004$. We used the quadratic approximation for the Stefan condition and Chorin's projection method. As we can see, the limbs grow faster than the concave parts of the interface. Also the fluid surface is moving faster there. This is due to the larger undercooling at the limbs and the temperature peaks at the concave parts, which can be seen especially in the contour plot in the right column of Figure 15. Here, the contour lines $T = -1.0, -0.9, \ldots, -0.1, 0.0, 0.01, 0.02, 0.03$ are plotted for $\rho_L = 2$.

4.3 Example 3: Solidification of water

As third example, we simulate the solidification of supercooled water on a microscopic scale, using the full mathematical model (34) – (47) including the pressure dependent and the kinetic term in the Gibbs–Thomson and the generalized Stefan condition. The physical parameters from [27] and [34] are given in Table 3.

quantity	symbol	value	unit
dynamic viscosity	μ	$1.79 \cdot 10^{-3}$	$\mathrm{kg\,m^{-1}s^{-1}}$
thermal expansion	α	$-6 \cdot 10^{-5}$	$\mathrm{K^{-1}}$
density of water	ρ_l	$1.00 \cdot 10^{3}$	$\mathrm{kg\,m^{-3}}$
density of ice	ρ_s	$9 \cdot 10^{2}$	$\mathrm{kg\,m^{-3}}$
thermal conductivity in water	k_l	$5.67 \cdot 10^{-1}$	$\mathrm{W\,K^{-1}m^{-1}}$
thermal conductivity in ice	k_s	2.26	$\mathrm{W\,K^{-1}m^{-1}}$
specific heat conductivity of water	c_l	$4.2 \cdot 10^{3}$	$\mathrm{J\,K^{-1}kg^{-1}}$
specific heat conductivity of ice	c_s	$1.9 \cdot 10^{3}$	$\mathrm{J\,K^{-1}kg^{-1}}$
surface tension water/air	γ_2	$7.3 \cdot 10^{-2}$	$\mathrm{N\,m^{-1}}$
surface tension water/ice	γ_1	$2.9 \cdot 10^{-2}$	$\mathrm{N\,m^{-1}}$
latent heat per unit mass	L	$3.07 \cdot 10^{5}$	$\mathrm{J\,kg^{-1}}$
melting temperature	T_m	273	K
kinetic coefficient in Gibbs–Thomson	a	$2.06 \cdot 10^{-2}$	$\mathrm{m^4\,K^{-1}kg^{-1}s^{-1}}$
parameter of heat flux at the fluid surface	h	150	$\mathrm{W\,K^{-1}m^{-2}}$

Table 3: Physical parameters of water and ice at $T = 273\mathrm{K}$

We consider a quadratic domain $[0, a] \times [0, a]$ with $a = 10\mu\mathrm{m}$. At the bottom, there is a layer of ice. The solid-liquid interface is a plane with a slight perturbation. It has the form

$$\Gamma_1(0) := \left\{ (x, y) \,\middle|\, y = a \left(0.0625 - 0.0125 \cos\left(\frac{2\,\pi\,x}{a} \right) \right) \right\} \tag{77}$$

at $t = 0$.

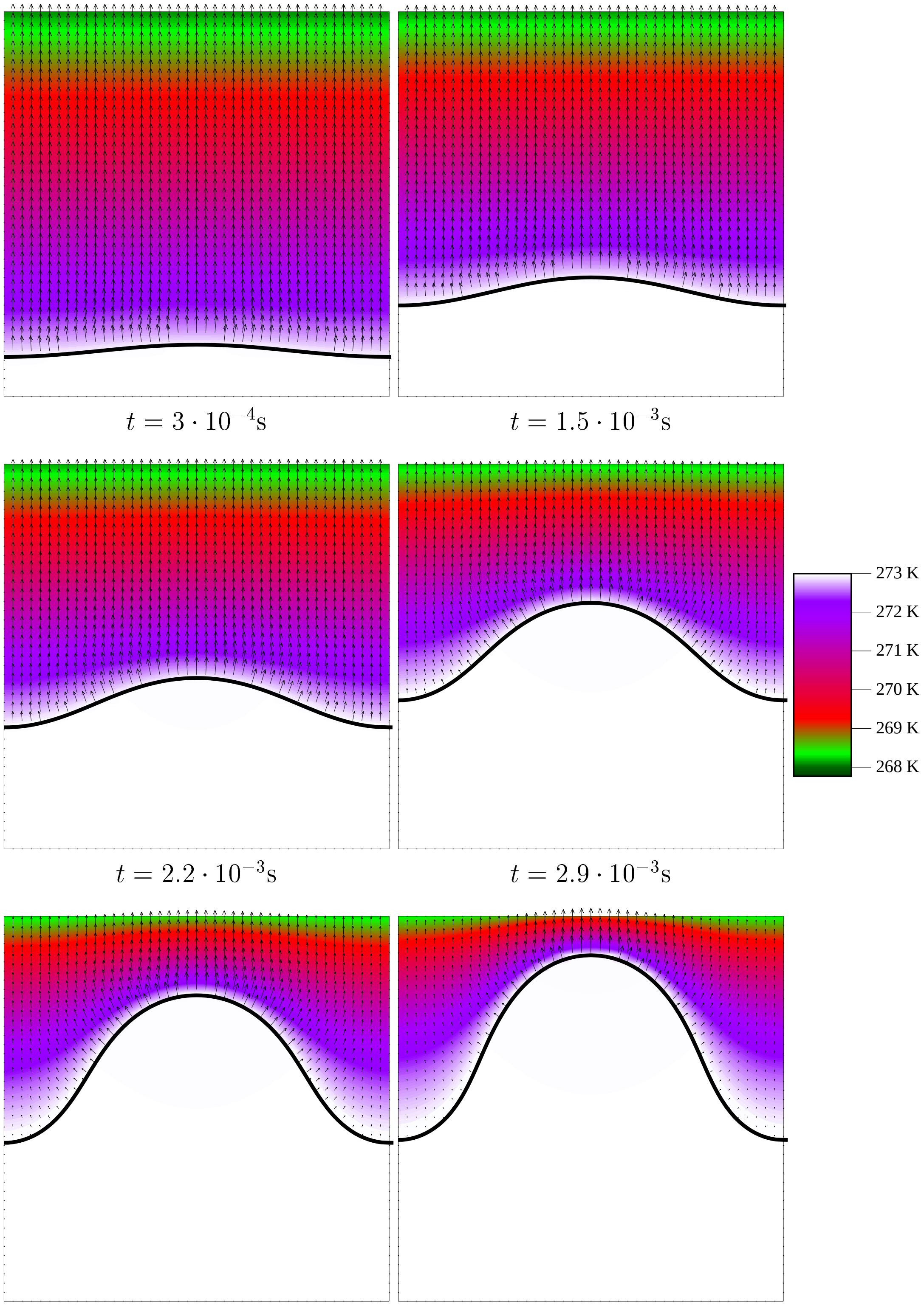

$t = 3 \cdot 10^{-4}$s $t = 1.5 \cdot 10^{-3}$s

$t = 2.2 \cdot 10^{-3}$s $t = 2.9 \cdot 10^{-3}$s

$t = 3.25 \cdot 10^{-3}$s $t = 3.4 \cdot 10^{-3}$s

Figure 16: Example 3: Color-coded temperature, velocity plot and solid-liquid interface at several time steps, the length of the velocity vectors is not uniformly scaled

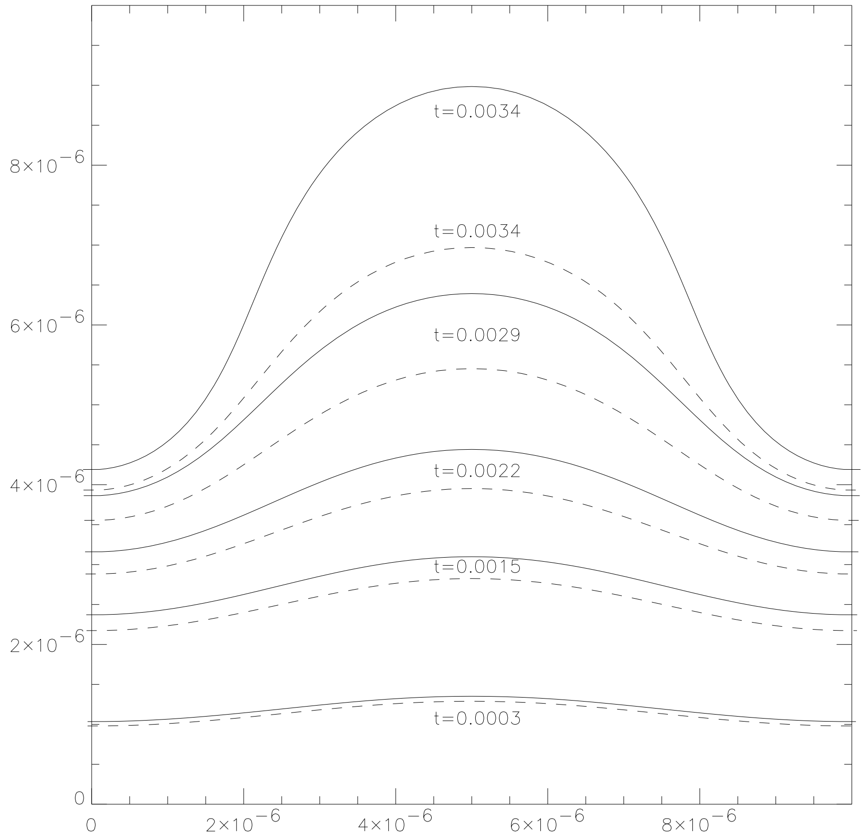

Figure 17: Example 3: Solid-liquid interface at several time-steps, with (solid lines) and without (dashed lines) density changes

The initial temperature is

$$T^{(0)} = T_m + \Delta T(e^{-50y/a} - 1) \tag{78}$$

in the fluid and $T = T_m = 273\text{K}$ in the solid. The degree of supercooling is $\Delta T = 5K$. As boundary condition for the temperature, we use $T = T_m$ at the bottom, $T = T_m - \Delta T = 268K$ at the top, and adiabatic boundary conditions at the left and the right boundary. For the velocity, we apply the slip condition $u = 0, \partial v/\partial n = 0$ which is used for symmetry axes at the left and right wall. At the top, we apply the outflow condition $\partial\vec{v}/\partial n = 0$.
For the computations, we used a grid with 40×40 cells and a time step size $\delta t = 8 \cdot 10^{-6}\text{s}$. For the time discretization of the momentum equations, we use the SIMPLE scheme, because the stability condition (62) for the explicit Chorin scheme would require step sizes $\delta t < 9 \cdot 10^{-9}\text{s}$. In Figure 16, we show the solidification process and see that the convex parts of the interface grow much faster than the concave ones. In Figure 17, we compare the simulation results of our enlarged model and a standard model without density changes, i.e. $\rho_S = \rho_L = 1000\text{kg}\,\text{m}^{-3}$.

We see that the simulation with density change shows a quite faster solidification than the simulation with equal densities in fluid and water. Thus, for this physical situation, the additional simulation of the fluid dynamics has a substantial effect on the simulation of the whole solidification process. We suppose that the reason for the faster solidification under consideration of density changes is the following: the latent heat released during solidification is carried away by the fluid flow. Thus, the undercooling of the interface is larger compared to the simulation without density changes, resulting in a higher speed of the interface.

4.4 Example 4: Dendritic Solidification

Finally, we present an example of dendritic solidification. Here, the constants in the Gibbs–Thomson condition (64) are assumed to depend on the direction of the normal of the solid-liquid interface, namely

$$\varepsilon_\kappa = \varepsilon_V = \varepsilon(\vec{n}) = \varepsilon_0 \,(1 + b\,\cos(k\,\varphi)), \tag{79}$$

where φ denotes the angle between the normal $\vec{n}$ and the x-axis, see [2], [7], [23], [29]. Using an anisotropy frequency $k = 4$, the crystal growths much faster in diagonal direction than parallel to the axes. This is shown in Figure 18 where we plot the solid-liquid interface at several time-steps.

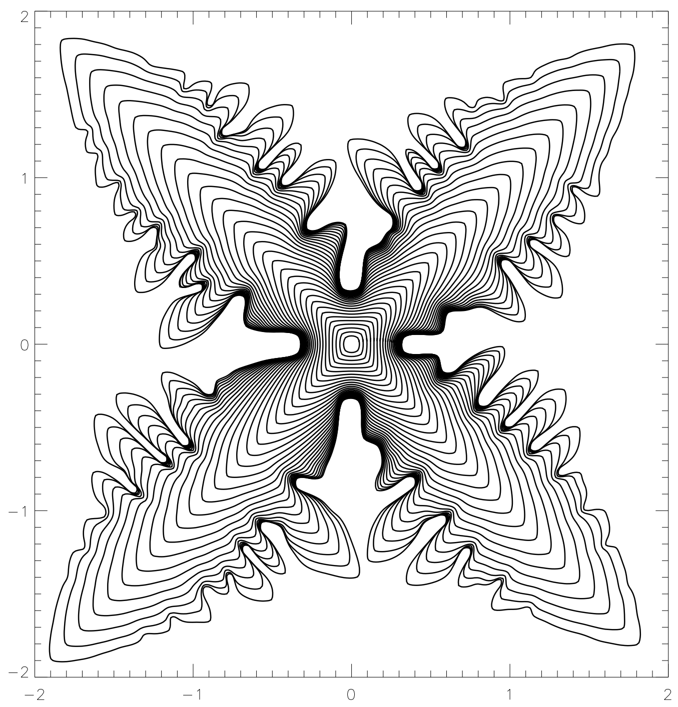

Figure 18: Example 4: Dendritic solidification, solid-liquid interface at $t = m \cdot 0.004, m = 1, \ldots, 31$

For the computation, we divided the domain $\Omega_0 := [-2, 2] \times [-2, 2]$ into 200×200 grid cells using the time stepsize $\delta t = 0.00001$. The initial radius of the seed was $R_{1,0} = 0.04$. The temperature on the boundary of the domain is $T|_{\Gamma_3} = -1.0$. Further parameters were $\varepsilon_0 = 0.001$, $k = 4$, $b = 0.6$, $L = 1$. Here, we restrict ourselves to the model without density changes and omit the calculation of the fluid flow. It turned out that to obtain significant results for the flow calculation, adaptive grid techniques are required. However, the dendritic pattern of the crystal can be also obtained on an equidistant grid for the temperature solver.

5 Conclusions

In this paper, we presented a new model for the solidification of a supercooled melt, including fluid dynamical effects caused by a density change during solidification. Due to these kinetic effects, some additional terms including pressure and velocity enter the Gibbs–Thomson and the Stefan condition at the solid-liquid interface.

Furthermore, we developed a numerical algorithm based on finite difference discretizations on a fixed grid, whose cells are divided into solid, liquid and empty cells by the surface marker method. The numerical results showed that the algorithm has a convergence rate of order $O(h^{3/2})$. For the physical parameters of water, a significant difference between the solidification speed in the simulations with and without consideration of density changes was observed.

However, the approach has its limitations and needs further improvement. For example, higher order schemes can be used for the discretization in time and space. Moreover, the efficiency of the solver in the pressure correction equation and the convection-diffusion equations in the SIMPLE scheme should be enhanced. Here, instead of the SOR algorithm, a multigrid method might be applied. Since we are dealing with complicated geometries and convection-diffusion equations, standard multigrid cannot be used here. We need algebraic multigrid methods (AMG), [19], or other specialized multigrid techniques, [3], [4], instead. Additionally, for improved efficiency and accuracy, adaptive refinement strategies are necessary to resolve the heat and fluid flow at the interface more properly. This is especially important in the case of dendritic growth because of the fine crystal tips and fluid channels in between.

Then, the generalization of the numerical method to the three-dimensional case would be advantageous. Here, the treatment of the free boundaries gets more complicated since the free surface is two-dimensional and no more a one-dimensional manifold. Thus, neighboring particles on the boundaries cannot be identified by their position in the data structure anymore. Additional information stored in vertex-edge-face (vef) graphs is required.

Finally, also the model might be generalized by assuming that the solid is not at rest but is allowed to float and to be moved by the fluid flow. Additionally, effects of elasticity are to be modeled, especially for contracting substances, where cracks might arise.

This will be future work.

Acknowledgement

The authors wish to thank I.G. Götz for his helpful discussions concerning the modeling of the problem and Chr. Morkel for discussions on the physical aspects of solidification processes.

References

[1] V. Alexiades and A. Solomon, *Mathematical Modelling of Melting and Freezing Processes*, Hemisphere Publishing, Washington DC, 1993.

[2] R. Almgren, *Variational algorithms and pattern formation in dendritic solidification*, J. Comp. Phys., 106 (1993), pp. 337–354.

[3] R. Bank and J. Xu, *A hierarchical basis multi-grid method for unstructured grids*, in Fast Solvers for Flow Problems, Proc. of the 10th GAMM Seminar, W. Hackbusch and G. Wittum, eds., Vieweg, 1995.

[4] ——, *An algorithm for coarsening unstructured meshes*, Numer. Math., 73 (1996), pp. 1–36.

[5] B. Bazalii and S. Degtyarev, *On classical solvability of the multidimensional stefan problem for convective motion of a viscous incompressible fluid*, Math. USSR Sbornik, 60 (1988), pp. 1–17.

[6] E. Becker and W. Bürger, *Kontinuumsmechanik*, Teubner, Stuttgart, 1975.

[7] E. Ben-Jacob, N. Goldenfeld, J. Langer, and G. Schön, *String models of interfacial pattern formation*, Physica D, 12 (1984), pp. 245–252.

[8] O. Caginalp and E. Socolovsky, *Computation of sharp phase by spreading: The planar and spherically symmetric cases*, J. Comp. Phys., 95 (1991), pp. 85–100.

[9] ——, *Phase field computations of single-needle crystals, crystal growth, and motion by mean curvature*, SIAM J. Sci. Comp., 15 (1994), pp. 106–126.

[10] C. Charach, B. Zaltzman, and I. Götz, *Interfacial kinetics effect in planar solidification problems without initial undercooling*, Mathematical Models and Methods in Appl. Sci., 4 (331–354), p. 1994.

[11] C. Charach and A. Zemel, *Irreversible thermodynamics of phase change heat transfer: Basic prinziples and applications to latent heat storage*, Open Systems & Information Dynamics, 1 (1992), pp. 423–458.

[12] S. Chen, D. Johnson, and P. Raad, *The surface marker method*, in Computational Modelling of Free and Moving Boundary Problems, Vol 1 Fluid Flow, L. Wrobel and C. Brebbia, eds., de Gruyter, 1991, pp. 223–235.

[13] X. Chen and F. Reitich, *Local existence and uniqueness of solutions of the stefan problem with surface tension and kinetic undercooling*, J. Math. Analysis and Appl., 164 (164), pp. 350–362.

[14] A. Chorin, *Numerical solution of the Navier-Stokes-equations*, Math. Comput., 22 (1968), pp. 745–762.

[15] G. Fix and J. Lin, *Numerical simulations of nonlinear phase transitions – I. The isotropic case*, Nonlinear Analysis, 12 (1988), pp. 811–823.

[16] I. Götz and M. Primicerio, *Spherically symetric stefan problem with the gibbs–thomson law at the moving boundary*, Euro. J. of Appl. Math., 7 (1996), pp. 249–275.

[17] I. Götz and B. Zaltzman, *Two–phase stefan–problem with supercooling*, SIAM J. Math. Anal., 26 (1995), pp. 694–714.

[18] D. Gray and A. Giorgini, *On the validity of the Boussinesq approximation for liquids and gases*, Journal of Heat Mass Transfer, 19 (1976), pp. 545–551.

[19] M. Griebel, T. Neunhoeffer, and H. Regler, *Algebraic multigrid methods for the solution of the Navier-Stokes equations in complicated geometries*, TU München, Institut für Informatik, SFB-Report 342/01/96 A, http://wwwzenger.informatik.tu-muenchen.de/publikat/techber/sfb01_96.ps.gz, 1996.

[20] M. Gurtin, *Toward a nonequolibriumthermodynamics of two-phase materials*, Arch. Ration. Mech. Anal., 100 (1988), pp. 275–312.

[21] R. Hudspeth, R. Guenther, K. Roley, and W. McDougal, *Scaling thermal effects in radial flow*, Adv. in Water Resources, 15 (1992), pp. 107–116.

[22] S. Kaczmarz, *Angenäherte Auflösung von Systemen linearer Gleichungen*, Bulletin de l'Academie Polonaise des Sciences et Lettres, A35 (1937), pp. 355–357.

[23] R. Kobayashi, *Modeling and numerical simulations of dendritic crystal growth*, Physica D, 63 (1993), pp. 410–423.

[24] J. Langer, *Instabilities and pattern formation in crystal growth*, Reviews of Modern Physics, 52 (1980), pp. 1–28.

[25] T. Neunhoeffer, *Numerische Simulation von Erstarrungsprozessen unterkühlter Flüssigkeiten unter Berücksichtigung von Dichteunterschieden.* Dissertation, TU München, Institut für Informatik, 1997.

[26] S. Patankar and D. Spalding, *A calculation procedure for heat, mass and momentum transfer in three-dimensional parabolic flows*, Int. J. Heat Mass Transfer, 15 (1972), pp. 1787–1806.

[27] Q. Pham, *Effect of supercooling on freezing time due to dendritic growth of ice cristals*, Rev. Int. Froid, 12 (1989), pp. 295–300.

[28] E. Radkevich, *The gibbs–thomson correction and conditions for the existence of a classical solution of the modified stefan problem*, Soviet. Math. Dokl., 1 (1988), pp. 274–278.

[29] A. Schmidt, *Computation of three dimensional dendrites with finite elements*, J. Comp. Phys., 125 (1996), pp. 293–312.

[30] J. Sethian and J. Strain, *Crystal growth and dendritic soldification*, J. Comp. Phys., 98 (1992), pp. 231–253.

[31] G. Shortley and G. Weller, *Numerical solution of Laplace's equation*, J. Appl. Phys., 9 (1938), pp. 334–348.

[32] W. Shyy, H. Udaykumar, M. Rao, and R. Smith, *Computational Fluid Dynamics with Moving Boundaries*, Taylor & Francis, Washington DC, 1996.

[33] J. Smith, *Shape instabilities and pattern formation in solidification: A new method for numerical solution of the moving boundary problem*, J. Comp. Phys., 39 (1981), pp. 112–127.

[34] J. Sullivan, D. Lynch, and K. O'Neil, *Finite element simulation of planar instabilities during solidification of an undercooled melt*, Journal of Computational Physics, 69 (1987), pp. 81–111.

[35] K.-H. Tacke and A. Harnisch, *Finite difference enthalpy methods for dendritic growth*, in Computational Modelling of Free and Moving Boundary Problems, Vol 2 Heat Transfer, L. Wrobel and C. Brebbia, eds., de Gruyter, 1991, pp. 165–176.

[36] M. Tome and S. McKee, *GENSMAC: A computational marker and cell method for free surface flows in general domains*, J. Comp. Phys., 110 (1994), pp. 171–186.